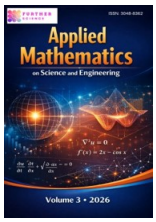
Applied Mathematics on Science and Engineering, 3(2):49–69, July-December: 2026.
DOI: https://doi.org/10.65036/amse326

Applied Mathematics on Science and Engineering
ISSN (Online): 3048-8362

Journal homepage: https://furthersci.org/journal-details.php?journal-id=49



Research Article

A Structure Preserving Numerical Study of a COVID–19 Transmission Model Using the Modified Patankar–Runge–Kutta Second-Order Method

Isaac Azure [1*], Emmanuel Owusu Ansah [1], Bright Emmanuel Owusu [1], Ishmael Takyi [1], Isabel Mensah [1], Prince Amponsah Kwabi [1] and Gabriel Obed Fosu [1]

[1] *Kwame Nkrumah University of Science and Technology, Department of Mathematics, KNUST, Kumasi, AK-03220, Ashanti Region, Ghana.*
[*] *Corresponding author: isaac.azure@knust.edu.gh*

Article Info

Keywords: *COVID-19, Mathematical models, Modified Patankar–Runge–Kutta schemes, Conservativity, Unconditional positivity.*

MSC 2020: *65L04, 92D30, 92D25.*

Received: *11.09.2026;*
Accepted: *20.10.2026;*
Published: *30.10.2026*

© 2026 by the author's. The terms and conditions of the Creative Commons Attribution (CC BY) license apply to this open access article.

Abstract

This study analyses a six-compartment (S, E, L, I, H, R) model for COVID-19 transmission that captures latent progression, hospitalization, disease-induced mortality, and waning immunity. The model's well-posedness was proved: solutions stayed positive and bounded, and the system had a positively invariant region. Using the next-generation matrix approach, the basic reproduction number was found to be $R_0 \approx 3.185$, which points to high transmissibility and an unstable disease-free equilibrium. To solve the model numerically, it was rewritten in production–destruction–rest form and the second-order Modified Patankar–Runge–Kutta (MPRK22) scheme applied to solve it. Comparing the resulting solution against the classical explicit Euler and fourth-order Runge–Kutta (RK4) methods, as well as the first-order MPRK1 scheme, across a wide range of time-step sizes, all four methods agreed closely when the time step size is small, but as the step size increased, however, Euler and RK4 began to produce negative population values; a clear biological impossibility; and RK4 eventually became numerically unstable at large step sizes. MPRK1 and MPRK22, by contrast, preserve positivity and remained stable across every step size tested, including the largest ones, without any loss of qualitative accuracy. These results confirm that MPRK22 is a robust, structure-preserving scheme well suited to long-term, policy-relevant COVID-19 modeling, particularly in settings where larger time steps are needed for computational efficiency.

1. Introduction

COVID-19 is caused by the novel coronavirus SARS-CoV-2, which is highly pathogenic and attacks the human respiratory system. The outbreak began in late December 2019, with the first cases detected at a seafood and wet animal market in Wuhan, Hubei Province, China. By January 2, 2020, 41 hospital patients had been diagnosed as infected. The virus spread quickly: on January 22, 2020, 571 cases were reported across 25 Chinese provinces, and by January 30, 2020, there had been 7,734 confirmed cases in China and 90 cases in 13 other countries, including Canada, India, Germany, France, the United States, and the UAE. As of October 31, 2020, almost 46 million cases and approximately 1.2 million deaths were reported globally, affecting all continents [1].

Ghana confirmed the first two COVID-19 cases on March 12, 2020, signifying the official start of the pandemic in the country. The government acted promptly, imposing a partial lockdown on March 30, 2020, which lasted 14 days and was later extended. During this

How To Cite: I. Azure, E.O. Ansah, B.E. Owusu, I. Takyi, I. Mensah, P.A. Kwabi, and G.O. Fosu. A Structure Preserving Numerical Study of a COVID–19 Transmission Model Using the Modified Patankar–Runge–Kutta Second-Order Method. *Applied Mathematics on Science and Engineering*, 3(2):49–69, 2026. https://doi.org/10.65036/amse326

period, extensive contact tracing and testing were undertaken, with approximately 86,000 people identified and 68,591 tests completed by April 19, 2020. Among those tested, 1,042 were positive, with 9 deaths and 99 recoveries reported at the time. Ghana was considered to have one of the highest testing rates per million people in Africa. The country also developed a comprehensive track and trace system, which, when paired with other public health initiatives, contributed to a reduction in mortality, with only 85 deaths reported by June 23, 2020. Local scientific and regulatory initiatives included genome sequencing of the virus, faster certification of hand sanitizers, and the creation of personal protective equipment and ventilators to address shortages [2].

According to [3], COVID-19 aerosols, the primary transmission medium, can be active on surfaces for up to 96 hours. Other coronaviruses, on the other hand, have an average life span of about nine hours. The growing number of COVID-19 cases renders the virus exceedingly contagious, raising health and economic concerns, particularly in underdeveloped countries with insufficient health facilities and equipment [4].

To battle the virus, Ghana, like many other countries, used a variety of public health measures, such as social distance, diagnostic screening, quarantine, isolation, and clinical management of infected individuals. On March 16, 2020, schools and universities were closed [5], and public gatherings were prohibited except for essential services. The Ministry of Health taught the public on COVID-19 prevention and transmission mechanisms using various media platforms, including newspapers, radio, and television [6].

As a result, various mathematical models have been developed worldwide to better explain and predict the dynamics of COVID-19 transmission. These models strive to give more effective disease control measures. One of these mathematical models is the six-compartment SAIUGR model, which is intended to depict several stages of COVID-19 progression and control, with each compartment representing a distinct demographic segment relevant to disease transmission and intervention measures. The model distinguishes between reported and unreported symptomatic cases, awarding a higher isolation rate to unreported patients once found in order to address under-reporting and prevent ongoing transmission [7]. Another study proposed a compartmental epidemic model called SAIRP, which splits the population into five separate compartments to reflect the dynamics of COVID-19 transmission. This compartmental structure allows the model to account for asymptomatic transmission, the influence of public health initiatives, and the possibility of temporary protection, creating a flexible framework for assessing and fitting COVID-19 epidemic data [8].

In this study, a COVID-19 model with compartments S, E, L, I, H, R suited for any country is developed taking into account all factors that influence the spread of the disease.The model splits the infected population into three separate compartments to suit current trends in disease infection. The Exposed (E) class represent early incubation, not yet infectious, the Latent (L) class represent a later pre-infectious stage closer to becoming infectious and the Infected (I)class, which follows the idea in literature [9], but vary with the inclusion of the Hospitalized (H) compartment and the transmissions from one compartment to the other. The system (1) is analyzed proving its positivity and boundedness showcasing its validity. The Modified Patankar-Runge-Kutta second-order scheme, which is a conservative and unconditionally positive scheme, is then used to demonstrate how to solve the system (1). A comparative analysis on positivity preservation on the Modified Patankar-Runge-Kutta (MPRK22) second-order scheme, Modified Patankar-Runge-Kutta (MPRK1) first-order scheme, Euler and Runge-Kutta fourth-order method is carried out using the system (1) as the bench-mark problem. The study explored the use of synthetic data which was generated specifically for the system (1) for simulation purposes. The aim of the comparison is to demonstrate the superiority of the MPRK22 over the traditional classical schemes [10].

The remaining part of the paper is divided into sections, with Section 2 presenting the Model Formulation which introduces a detailed procedure and assumptions leading to the development of the COVID-19 model. Section 3 presents an analysis of the model, giving a detailed proof of positivity, boundedness and invarient region. The section also presents the equilibrium points, disease-free equilibrium point and endemic equilibrium point of the model. Derivation of the basic reproduction number also form part of the section 3. The section 4 give a layout of the Modified Partankar-Runge-Kutta schemes, while section 5 breaks the model equation into production-destruction-rest terms and present them into the production matrix and the destruction-rest term vectors. The application of the MPRK1 and MPRK22 schemes to the COVID-19 model is presented in section 6. The Section 7 presents the numerical simulation results, and finally section 8 presents the concluding findings in the study.

2. Model Formulation

Figure 1 shows a compartmental deterministic model that describes the transmission dynamics of COVID-19 in a human population by dividing individuals into six epidemiological classes: susceptible S, exposed E, latent L, infectious I, hospitalised H, and recovered R. The exposed (E) and latent (L) compartments represent two biologically distinct pre-infectious stages. The exposed class corresponds to the early incubation period immediately after infection, where individuals are not yet committed to becoming infectious. The latent class represents a later stage in which individuals are closer to developing infectiousness and transition to the infectious class at a defined rate. This distinction introduces a more realistic delay in disease progression and improves the model's ability to capture incubation dynamics. Recruitment into the population occurs at a constant rate (Λ), with all new individuals entering the susceptible class. Susceptible individuals acquire infection through effective contact with infectious individuals at rate (βIS), after which they move into the exposed class. Natural mortality at rate (μ) affects all compartments, ensuring demographic realism. Additionally, recovered individuals may lose immunity and return to the susceptible class at rate (ϕ), capturing waning immunity and the possibility of reinfection.

The disease progression is structured to reflect the biological stages of COVID-19 infection [11]. Exposed individuals E represent those who are infected but not yet infectious, and they progress to the latent class L at rate (σ). Individuals in the latent class are infected and may develop symptoms or be detected, after which they move into the infectious class I at rate (γ_L). From the latent class, some individuals may also be directly hospitalised at rate (θ), reflecting early detection or rapid clinical deterioration, while others may recover directly at rate (ρ_L). These transitions allow the model to distinguish between pre-symptomatic infection, active infectiousness, and early clinical intervention [12].

The infectious and hospitalised compartments capture disease severity and clinical outcomes. Infectious individuals I may recover naturally at rate (γ_I), progress to hospitalisation at rate (θ_I), or experience disease-induced death at rate (δ_1) in addition to natural mortality. Hospitalised individuals H recover at rate (ρ_H) or die due to disease at rate (δ_2). All recovered individuals accumulate in the recovered class R, where they are subject to natural death and possible loss of immunity. A detailed description of all parameters used in the study is summarised in Table 1. Overall, the model incorporates infection transmission, disease progression, hospitalisation, recovery, mortality,

and immunity loss in a coherent framework that is suitable for both analytical study and numerical simulation of COVID-19 dynamics, particularly in settings such as Ghana where healthcare capacity and demographic structure play critical roles.

Table 1: Description of Parameters Used in the COVID-19 Model

Parameter	Description
Λ	Recruitment rate (new individuals entering the susceptible class)
μ	Natural death rate
β	Transmission rate from infectious individuals to susceptible individuals
σ	Progression rate from exposed (E) to latent (L) class
θ	Rate of progression from latent (L) to hospitalised (H)
θ_I	Rate of progression from infectious (I) to hospitalised (H)
ρ_L	Recovery rate of latent individuals ($L \to R$)
γ_L	Rate of progression from latent (L) to infectious (I)
γ_I	Recovery rate of infectious individuals ($I \to R$)
δ_1	Disease-induced death rate for infectious individuals (I)
δ_2	Disease-induced death rate for hospitalised individuals (H)
ρ_H	Recovery rate of hospitalised individuals ($H \to R$)
ϕ	Rate of loss of immunity, i.e. waning immunity ($R \to S$)

Based on the above assumptions, the model is described by the following system of ordinary differential equations:

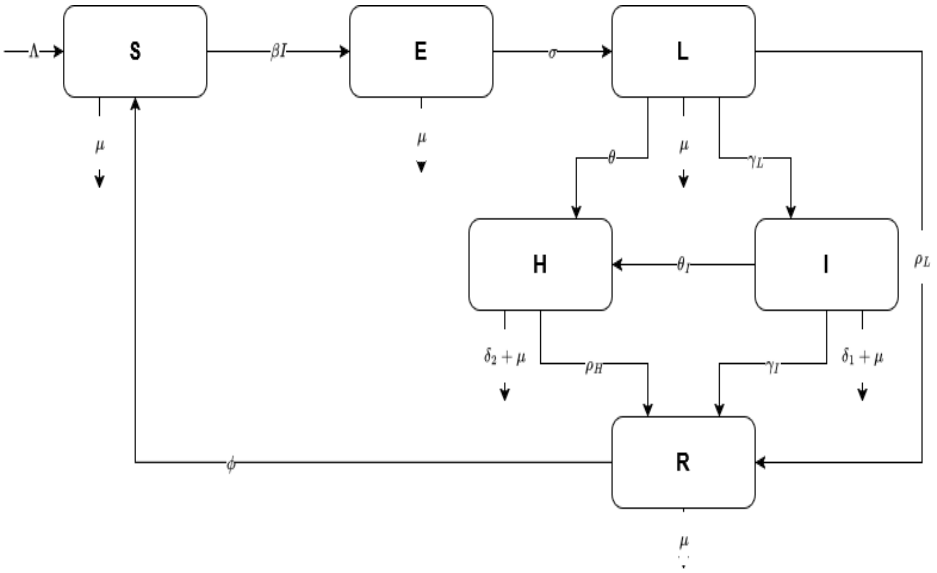


Figure 1: Generalized COVID-19 Model for the Selected Models

$$
\begin{aligned}
\frac{dS}{dt} &= \Lambda - \beta IS - \mu S + \phi R, \\
\frac{dE}{dt} &= \beta IS - \sigma E - \mu E, \\
\frac{dL}{dt} &= \sigma E - \rho_L L - \theta L - \gamma_L L - \mu L, \\
\frac{dI}{dt} &= \gamma_L L - \theta_I I - \gamma_I I - (\mu + \delta_1) I, \\
\frac{dH}{dt} &= \theta L + \theta_I I - \rho_H H - (\mu + \delta_2) H, \\
\frac{dR}{dt} &= \gamma_I I + \rho_H H + \rho_L L - \phi R - \mu R.
\end{aligned} \tag{1}
$$

Let the state vector for system (1) be

$$\mathbf{c} = (c_1, c_2, c_3, c_4, c_5, c_6)^T = (S, E, L, I, H, R)^T .$$

3. Model Analysis

In this section, we analyze the basic qualitative properties of system (1), namely positivity, boundedness, and the existence of a positively invariant region. These properties guarantee that the model is mathematically well-posed and epidemiologically meaningful [13, 14].

3.1. Positivity, Boundedness, and Invariant Region

Theorem 3.1 (Positivity, Boundedness, and Invariant Region)**.** *Let $c = (S,E,L,I,H,R)^T \in \mathbb{R}^6$ evolve according to system (1), with locally Lipschitz right-hand side $f : \mathbb{R}^6 \to \mathbb{R}^6$, and let*

$$N(t) = S(t)+E(t)+L(t)+I(t)+H(t)+R(t).$$

Then, for any initial condition $c(0) \in \mathbb{R}^6_+$:

- ***(i) Positivity.*** *The solution $c(t)$ satisfies $c(t) \in \mathbb{R}^6_+$ for all $t \geq 0$ on its interval of existence.*
- ***(ii) Boundedness.*** *The total population is bounded, with*

$$N(t) \leq N(0)e^{-\mu t} + \frac{\Lambda}{\mu}\left(1-e^{-\mu t}\right),$$

so that

$$\limsup_{t\to\infty} N(t) \leq \frac{\Lambda}{\mu}.$$

- ***(iii) Positive invariance.*** *Given (i) and (ii), the region*

$$\Omega = \left\{(S,E,L,I,H,R) \in \mathbb{R}^6_+ : N \leq \frac{\Lambda}{\mu}\right\}$$

is positively invariant under the flow of system (1); that is, if $c(0) \in \Omega$ then $c(t) \in \Omega$ for all $t \geq 0$.

Proof. **(i) Positivity.** Write system (1) as $\dot{c} = f(c)$. A system is said to be *quasipositive* on $\mathbb{R}^6_+$ if, for every i,

$$f_i(c) \geq 0 \quad \text{whenever } c \in \mathbb{R}^6_+ \text{ and } c_i = 0.$$

Quasipositivity verification. Recall that a locally Lipschitz vector field $f : \mathbb{R}^6 \to \mathbb{R}^6$ is said to be *quasipositive* on $\mathbb{R}^6_+$ if, for every index $i \in \{1,\ldots,6\}$,

$$c \in \mathbb{R}^6_+ \text{ and } c_i = 0 \quad \Longrightarrow \quad f_i(c) \geq 0.$$

By Nagumo's theorem, quasipositivity of a locally Lipschitz vector field is necessary and sufficient for $\mathbb{R}^6_+$ to be positively invariant under the associated flow. Since every right-hand side in system (1) is a polynomial (affine or bilinear) function of c, f is C^1 and hence locally Lipschitz on $\mathbb{R}^6$; it therefore suffices to verify quasipositivity componentwise on each boundary face $c_i = 0$.

Setting each state variable in turn to zero (with all remaining coordinates and all model parameters nonnegative) gives

$$f_1\big|_{S=0} = \Lambda + \phi R \geq 0, \tag{2}$$
$$f_2\big|_{E=0} = \beta IS \geq 0, \tag{3}$$
$$f_3\big|_{L=0} = \sigma E \geq 0, \tag{4}$$
$$f_4\big|_{I=0} = \gamma_L L \geq 0, \tag{5}$$
$$f_5\big|_{H=0} = \theta L + \theta_I I \geq 0, \tag{6}$$
$$f_6\big|_{R=0} = \gamma_I I + \rho_H H + \rho_L L \geq 0, \tag{7}$$

each of which holds automatically because all parameters and the remaining state variables are nonnegative on $\mathbb{R}^6_+$. In each case, every term in f_i involving c_i itself vanishes on the face $c_i = 0$, leaving only inflow contributions from other compartments – each a nonnegative parameter multiplied by a nonnegative state variable – so no compartment can be driven negative from its own zero boundary.
Since system (1) is quasipositive on $\mathbb{R}^6_+$, Nagumo's theorem guarantees that no trajectory starting in $\mathbb{R}^6_+$ can cross into the negative orthant, so $c(t) \in \mathbb{R}^6_+$ for all $t \geq 0$ on the interval of existence.

(ii) Boundedness. Summing the six equations of system (1), all inter-compartmental transfer terms cancel, leaving

$$\frac{dN}{dt} = \Lambda - \mu N - \delta_1 I - \delta_2 H \leq \Lambda - \mu N,$$

using the positivity established in (i) (so that $\delta_1 I,\ \delta_2 H \geq 0$). Thus $N(t)$ satisfies the linear differential inequality

$$\frac{dN}{dt} + \mu N \leq \Lambda.$$

By the (integral form of the) *Grönwall inequality* applied to this comparison equation, $N(t)$ is bounded above by the solution of the corresponding equality $\dot{y} = \Lambda - \mu y$, $y(0) = N(0)$, namely

$$N(t) \leq y(t) = N(0)e^{-\mu t} + \frac{\Lambda}{\mu}\left(1-e^{-\mu t}\right).$$

Letting $t \to \infty$, the transient terms vanish and

$$\limsup_{t\to\infty} N(t) \le \frac{\Lambda}{\mu}.$$

(iii) Positive invariance of Ω. Let $c(0) \in \Omega$, i.e. $c(0) \in \mathbb{R}^6_+$ with $N(0) \le \Lambda/\mu$. By part (i), $c(t) \in \mathbb{R}^6_+$ for all $t \ge 0$. By part (ii),

$$N(t) \le N(0)e^{-\mu t} + \frac{\Lambda}{\mu}\left(1 - e^{-\mu t}\right) \le \frac{\Lambda}{\mu}e^{-\mu t} + \frac{\Lambda}{\mu}\left(1 - e^{-\mu t}\right) = \frac{\Lambda}{\mu},$$

where the middle inequality uses $N(0) \le \Lambda/\mu$. Hence $N(t) \le \Lambda/\mu$ for all $t \ge 0$, and together with $c(t) \in \mathbb{R}^6_+$ this gives $c(t) \in \Omega$ for all $t \ge 0$. Consequently, Ω is positively invariant under the flow of system (1), and it suffices to study the model's dynamics within Ω. □

3.2. Equilibrium Points of the Model

In this subsection, we determine the equilibrium points of system (1), namely the disease-free equilibrium (DFE) and the endemic equilibrium (EE). These equilibrium states play a fundamental role in understanding the qualitative behavior of the COVID-19 transmission dynamics.

3.2.1. Disease-Free Equilibrium Point

The disease-free equilibrium point, denoted by ε, corresponds to the state at which there is no infection present in the population. At this equilibrium, all disease-related compartments vanish, that is,

$$E = L = I = H = R = 0.$$

This situation represents a completely disease-free population where no individuals are exposed, latent, infectious, hospitalised, or recovered.

Substituting these values into system (1) and setting the time derivatives equal to zero yields

$$\frac{dS}{dt} = \Lambda - \mu S = 0.$$

Solving for S, we obtain

$$S^* = \frac{\Lambda}{\mu}.$$

Therefore, the disease-free equilibrium point is given by

$$\varepsilon = \left(\frac{\Lambda}{\mu}, 0, 0, 0, 0, 0\right).$$

Biologically, this equilibrium describes a population in which all individuals are susceptible and the population size is regulated by the balance between recruitment and natural mortality. The stability of this equilibrium is typically governed by the basic reproduction number R_0, which determines whether an introduced infection can invade the population.

3.3. Derivation of the Basic Reproduction Number R_0

The basic reproduction number R_0 is defined as the expected number of secondary infections produced by a single infectious individual introduced into a completely susceptible population [15, 16]. In this subsection, we derive R_0 using the next-generation matrix method.

For the present model, the disease transmission pathway follows the progression

$$E \longrightarrow L \longrightarrow I,$$

and only individuals in the infectious class I generate new infections through the nonlinear incidence term βIS. Accordingly, we consider the infected subsystem

$$x = (E, L, I, H)^T.$$

The system is linearized at the disease-free equilibrium (DFE),

$$\nabla = (S^*, 0, 0, 0, 0, 0), \qquad S^* = \frac{\Lambda}{\mu}.$$

New Infection Matrix

Let $F(x)$ denote the vector of new infection terms. Since only the infectious compartment contributes to new infections, we have

$$F(x) = \begin{pmatrix} \beta S^* I \\ 0 \\ 0 \\ 0 \end{pmatrix}.$$

The Jacobian matrix of F evaluated at the DFE is therefore given by

$$F = \begin{pmatrix} 0 & 0 & \beta S^* & 0 \\ 0 & 0 & 0 & 0 \\ 0 & 0 & 0 & 0 \\ 0 & 0 & 0 & 0 \end{pmatrix}.$$

Although hospitalized individuals belong to the infected subsystem, they do not generate new infections, which explains the zero row in the matrix F.

Transition Matrix

Let $V(x)$ represent the transition vector, defined as the difference between outflows and inflows for each infected compartment, excluding new infections [17]. The corresponding components are

$$\begin{aligned} V_1 &= (\sigma+\mu)E, \\ V_2 &= -\sigma E + (\rho_L+\theta+\gamma_L+\mu)L, \\ V_3 &= -\gamma_L L + (\theta_I+\gamma_I+\mu+\delta_1)I, \\ V_4 &= -\theta L - \theta_I I + (\rho_H+\mu+\delta_2)H. \end{aligned}$$

The Jacobian matrix of V at the DFE is

$$V = \begin{pmatrix} \sigma+\mu & 0 & 0 & 0 \\ -\sigma & P_L & 0 & 0 \\ 0 & -\gamma_L & P_I & 0 \\ 0 & -\theta & -\theta_I & P_H \end{pmatrix},$$

where

$$P_L = \rho_L+\theta+\gamma_L+\mu, \quad P_I = \theta_I+\gamma_I+\mu+\delta_1, \quad P_H = \rho_H+\mu+\delta_2.$$

Next-Generation Matrix

The next-generation matrix is defined as

$$K = FV^{-1}. \tag{8}$$

Since F has only one nonzero entry, located at position $(1,3)$, the product $K = FV^{-1}$ has nonzero entries only in its first row:

$$K_{1j} = F_{13}\,(V^{-1})_{3j}, \qquad j = 1,2,3,4, \qquad \text{and} \qquad K_{ij} = 0 \text{ for } i \neq 1.$$

A matrix of this form (only the first row nonzero) has characteristic polynomial $\lambda^3(\lambda - K_{11}) = 0$, so its eigenvalues are $0,0,0,K_{11}$. Consequently,

$$\rho(K) = K_{11} = F_{13}\,(V^{-1})_{31} = \beta S^*\,(V^{-1})_{31}.$$

Hence R_0 requires the $(3,1)$-entry of V^{-1}, i.e. the third component of the *first* column of V^{-1}, obtained by solving

$$Vy = e_1, \qquad e_1 = (1,0,0,0)^T.$$

Solving sequentially (using the lower-triangular structure of V),

$$\begin{aligned} (\sigma+\mu)y_1 = 1 \quad &\Rightarrow \quad y_1 = \frac{1}{\sigma+\mu}, \\ -\sigma y_1 + P_L y_2 = 0 \quad &\Rightarrow \quad y_2 = \frac{\sigma y_1}{P_L} = \frac{\sigma}{(\sigma+\mu)P_L}, \\ -\gamma_L y_2 + P_I y_3 = 0 \quad &\Rightarrow \quad y_3 = \frac{\gamma_L y_2}{P_I} = \frac{\sigma\gamma_L}{(\sigma+\mu)P_L P_I}, \\ -\theta y_2 - \theta_I y_3 + P_H y_4 = 0 \quad &\Rightarrow \quad y_4 = \frac{\theta y_2 + \theta_I y_3}{P_H}. \end{aligned}$$

Thus the first column of V^{-1} is

$$(V^{-1})_{\cdot 1} = \begin{pmatrix} \dfrac{1}{\sigma+\mu} \\ \dfrac{\sigma}{(\sigma+\mu)P_L} \\ \dfrac{\sigma\gamma_L}{(\sigma+\mu)P_L P_I} \\ y_4 \end{pmatrix}, \qquad \text{so that} \qquad (V^{-1})_{31} = \frac{\sigma\gamma_L}{(\sigma+\mu)P_L P_I}.$$

Expression for R_0

Substituting $(V^{-1})_{31}$ into $\rho(K) = \beta S^*(V^{-1})_{31}$ gives the basic reproduction number directly:

$$R_0 = \rho(K) = \beta S^* \frac{\sigma\gamma_L}{(\sigma+\mu)P_L P_I} = \beta S^* \frac{\sigma}{\sigma+\mu} \cdot \frac{\gamma_L}{\rho_L+\theta+\gamma_L+\mu} \cdot \frac{1}{\theta_I+\gamma_I+\mu+\delta_1}. \tag{9}$$

This expression has a natural epidemiological interpretation as a product of three factors: $\frac{\sigma}{\sigma+\mu}$ is the probability that an exposed individual survives natural death and progresses to the latent class, $\frac{\gamma_L}{P_L}$ is the probability that a latent individual survives (and is not hospitalised or otherwise removed) and progresses to the infectious class, and $T_I = \frac{1}{P_I}$ is the mean sojourn time in the infectious class. Multiplying these survival/transition probabilities by the transmission rate βS^* and the mean infectious period recovers exactly the expression above, confirming the next-generation-matrix result.

This quantity fully characterises the threshold behaviour of the model and determines whether COVID-19 can invade and persist in the population. Substituting the parameter values in Table 2 into the expression for the basic reproduction number, R_0, This gives an output result of $R_0 \approx 3.185$, indicating that the disease-free equilibrium is unstable and that, in the absence of additional interventions, each infectious individual generates approximately three secondary infections in a wholly susceptible population. Consequently, the disease-free equilibrium is unstable and sustained transmission of COVID-19 is expected under these parameter settings. Epidemiologically, $R_0 > 1$ confirms the potential for rapid outbreak growth in the absence of effective control measures, highlighting the need for interventions such as reduced transmission, faster isolation, or increased recovery rates to bring R_0 below unity.

3.4. Sequential Solution of the Endemic Equilibrium

Recall the equilibrium system obtained by setting the right-hand sides of system (1) to zero, and recall the shorthand notation already introduced in the derivation of R_0:

$$P_L = \rho_L+\theta+\gamma_L+\mu, \qquad P_I = \theta_I+\gamma_I+\mu+\delta_1, \qquad P_H = \rho_H+\mu+\delta_2.$$

$$\begin{aligned}
\Lambda - \beta I^{**}S^{**} - \mu S^{**} + \phi R^{**} &= 0,\\
\beta I^{**}S^{**} - (\sigma+\mu)E^{**} &= 0,\\
\sigma E^{**} - P_L L^{**} &= 0,\\
\gamma_L L^{**} - P_I I^{**} &= 0,\\
\theta L^{**} + \theta_I I^{**} - P_H H^{**} &= 0,\\
\gamma_I I^{**} + \rho_H H^{**} + \rho_L L^{**} - (\phi+\mu)R^{**} &= 0.
\end{aligned} \tag{10}$$

For the purpose of easy reference to the individual equations in the system (10), the equations were labeled (E1)–(E6). Because the system is triangular in structure (each new equation introduces exactly one new unknown), it can be solved sequentially, working from (E4) upward and then back down through (E5)–(E6).

Step 1 – Latent class L^{**} from (E4).

$$\gamma_L L^{**} = P_I I^{**} \quad \Longrightarrow \quad L^{**} = \frac{P_I}{\gamma_L} I^{**}.$$

Step 2 – Exposed class E^{**} from (E3).

$$\sigma E^{**} = P_L L^{**} = P_L \cdot \frac{P_I}{\gamma_L} I^{**} \quad \Longrightarrow \quad E^{**} = \frac{P_L P_I}{\sigma\gamma_L} I^{**}.$$

Step 3 – Susceptible class S^{**} from (E2).

$$\beta I^{**}S^{**} = (\sigma+\mu)E^{**} \quad \Longrightarrow \quad S^{**} = \frac{(\sigma+\mu)E^{**}}{\beta I^{**}} = \frac{(\sigma+\mu)P_L P_I}{\sigma\gamma_L\beta}.$$

Notably, the factor I^{**} cancels, so S^{**} is a *constant*, independent of the equilibrium infection level. Recalling the expression derived in Section 3.2,

$$R_0 = \beta S^* \frac{\sigma}{\sigma+\mu} \cdot \frac{\gamma_L}{P_L} \cdot \frac{1}{P_I}, \qquad S^* = \frac{\Lambda}{\mu},$$

this constant can be rewritten compactly as

$$S^{**} = \frac{S^*}{R_0} = \frac{\Lambda}{\mu R_0}.$$

Step 4 – Hospitalised class H^{**} from (E5).

$$P_H H^{**} = \theta L^{**} + \theta_I I^{**} = \left(\theta \frac{P_I}{\gamma_L} + \theta_I\right) I^{**} \quad \Longrightarrow \quad H^{**} = \frac{\theta P_I + \theta_I \gamma_L}{\gamma_L P_H} I^{**}.$$

Step 5 – Recovered class R^{**} from (E6).

Substituting L^{**} and H^{**},

$$(\phi+\mu)R^{**} = \gamma_I I^{**} + \rho_H H^{**} + \rho_L L^{**} = \left[\gamma_L\gamma_I + \rho_L P_I + \rho_H \frac{\theta P_I + \theta_I \gamma_L}{P_H}\right] \frac{I^{**}}{\gamma_L}.$$

Define the constant

$$\Psi := \gamma_L\gamma_I + \rho_L P_I + \rho_H \frac{\theta P_I + \theta_I \gamma_L}{P_H},$$

so that

$$R^{**} = \frac{\Psi}{\gamma_L(\phi+\mu)} I^{**}. \tag{11}$$

Step 6 Closing the loop with (E1).

All quantities except I^{**} itself have now been eliminated. Insert S^{**} (constant) and $R^{**} = \dfrac{\Psi}{\gamma_L(\phi+\mu)} I^{**}$ into (E1):

$$\Lambda - \mu S^{**} - \beta I^{**} S^{**} + \phi \frac{\Psi}{\gamma_L(\phi+\mu)} I^{**} = 0,$$

$$\Lambda - \mu S^{**} = I^{**}\left[\beta S^{**} - \frac{\phi\Psi}{\gamma_L(\phi+\mu)}\right].$$

Hence

$$I^{**} = \frac{\Lambda - \mu S^{**}}{\beta S^{**} - \dfrac{\phi\Psi}{\gamma_L(\phi+\mu)}}. \tag{12}$$

3.5. Existence of a Unique Endemic Equilibrium: the Role of R_0

Using $S^{**} = \Lambda/(\mu R_0)$ from Step 3, the numerator of (12) simplifies to

$$\Lambda - \mu S^{**} = \Lambda - \mu \cdot \frac{\Lambda}{\mu R_0} = \Lambda\left(1 - \frac{1}{R_0}\right) = \frac{\Lambda(R_0-1)}{R_0}. \tag{13}$$

For the denominator, note from the definition of R_0 that $\beta S^* = \dfrac{R_0(\sigma+\mu)P_L P_I}{\sigma\gamma_L}$, and since $S^{**} = S^*/R_0$,

$$\beta S^{**} = \frac{\beta S^*}{R_0} = \frac{(\sigma+\mu)P_L P_I}{\sigma\gamma_L}.$$

Thus the denominator of (12) is the parameter-only constant

$$D := \beta S^{**} - \frac{\phi\Psi}{\gamma_L(\phi+\mu)} = \frac{(\sigma+\mu)P_L P_I}{\sigma\gamma_L} - \frac{\phi\Psi}{\gamma_L(\phi+\mu)}, \tag{14}$$

which is independent of I^{**} and is strictly positive under biologically reasonable parameter regimes (the direct progression, recovery and mortality outflows represented by $(\sigma+\mu)P_L P_I$ dominate the feedback contribution of waning immunity $\phi\Psi$ returning individuals to S). Combining (12)– (14),

$$I^{**} = \frac{\Lambda(R_0-1)}{R_0 D}, \qquad D > 0. \tag{15}$$

Interpretation. Equation (15) shows explicitly that:

- If $R_0 > 1$, then $I^{**} > 0$, and consequently, since $L^{**}, E^{**}, H^{**}, R^{**}$ are each nonnegative constant multiples of I^{**} (Steps 1, 2, 4, 5) and $S^{**} = \Lambda/(\mu R_0) > 0$ (Step 3), *all* equilibrium components are strictly positive. Hence a biologically feasible endemic equilibrium $\nabla^{**} = (S^{**}, E^{**}, L^{**}, I^{**}, H^{**}, R^{**})$ exists, and it is unique because every component in (15) and Steps 1–5 is uniquely and explicitly determined by the model parameters.
- If $R_0 \leq 1$, then $I^{**} \leq 0$ from (15), which is not biologically admissible; the only equilibrium consistent with nonnegativity in this regime is the disease-free equilibrium $\varepsilon = (\Lambda/\mu, 0, 0, 0, 0, 0)$.
- If $R_0 = 1$ exactly, (15) gives $I^{**} = 0$, so the endemic equilibrium coalesces with the disease-free equilibrium, marking the threshold (transcritical) bifurcation point.

Therefore, the existence of a unique, strictly positive endemic equilibrium for system (1) is guaranteed if and only if $R_0 > 1$, consistent with the standard threshold theory of compartmental epidemic models.

3.6. Local Stability of the Endemic Equilibrium

Having established, in Sections 3.3–3.4, the existence and uniqueness of the endemic equilibrium $\nabla^{**} = (S^{**}, E^{**}, L^{**}, I^{**}, H^{**}, R^{**})$ whenever $R_0 > 1$, we now examine its local asymptotic stability. This is done in the standard way, by linearizing system (1) about ∇^{**} and analyzing the eigenvalues of the resulting Jacobian matrix.

3.6.1. The Jacobian Matrix

Writing system (1) as $\dot{c} = f(c)$ with $c = (S, E, L, I, H, R)^T$, the Jacobian $J(c) = \partial f / \partial c$ is

$$J(c) = \begin{pmatrix} -(\beta I + \mu) & 0 & 0 & -\beta S & 0 & \phi \\ \beta I & -(\sigma + \mu) & 0 & \beta S & 0 & 0 \\ 0 & \sigma & -P_L & 0 & 0 & 0 \\ 0 & 0 & \gamma_L & -P_I & 0 & 0 \\ 0 & 0 & \theta & \theta_I & -P_H & 0 \\ 0 & 0 & \rho_L & \gamma_I & \rho_H & -(\phi + \mu) \end{pmatrix}, \tag{16}$$

with P_L, P_I, P_H as in Section 3.5. Evaluating $J(c)$ at the endemic equilibrium ∇^{**} and writing $a = \beta S^{**}$, $b = \beta I^{**}$ gives the constant matrix

$$J^{**} = \begin{pmatrix} -(b + \mu) & 0 & 0 & -a & 0 & \phi \\ b & -(\sigma + \mu) & 0 & a & 0 & 0 \\ 0 & \sigma & -P_L & 0 & 0 & 0 \\ 0 & 0 & \gamma_L & -P_I & 0 & 0 \\ 0 & 0 & \theta & \theta_I & -P_H & 0 \\ 0 & 0 & \rho_L & \gamma_I & \rho_H & -(\phi + \mu) \end{pmatrix}. \tag{17}$$

3.6.2. Characteristic Polynomial: Direct Derivation

Local asymptotic stability of ∇^{**} holds if and only if every eigenvalue λ of J^{**} satisfies $\mathrm{Re}(\lambda) < 0$. Introduce the shorthand

$$X_1 = \lambda + b + \mu,\ X_2 = \lambda + \sigma + \mu,\ X_3 = \lambda + P_L,\ X_4 = \lambda + P_I,\ X_5 = \lambda + P_H,\ X_6 = \lambda + \phi + \mu, \tag{18}$$

and set $M(\lambda) := \lambda I - J^{**}$, so that $P(\lambda) = \det M(\lambda)$ (equivalently $P(\lambda) = \det(J^{**} - \lambda I)$, since $\det(J^{**} - \lambda I) = (-1)^6 \det M(\lambda) = \det M(\lambda)$ for the even dimension $n = 6$). Explicitly,

$$M(\lambda) = \begin{pmatrix} X_1 & 0 & 0 & a & 0 & -\phi \\ -b & X_2 & 0 & -a & 0 & 0 \\ 0 & -\sigma & X_3 & 0 & 0 & 0 \\ 0 & 0 & -\gamma_L & X_4 & 0 & 0 \\ 0 & 0 & -\theta & -\theta_I & X_5 & 0 \\ 0 & 0 & -\rho_L & -\gamma_I & -\rho_H & X_6 \end{pmatrix}. \tag{19}$$

Step 1 (Expansion along column 6). Column 6 of $M(\lambda)$ has exactly two nonzero entries: $-\phi$ in row 1 and X_6 in row 6. Hence

$$P(\lambda) = (-\phi) C_{16} + X_6 C_{66}, \tag{20}$$

where $C_{16} = (-1)^{1+6} \det M_{16}$ and $C_{66} = (-1)^{6+6} \det M_{66}$, and M_{ij} denotes the minor obtained by deleting row i and column j of $M(\lambda)$.

Step 2 (The M_{66} minor: the (S, E, L, I, H) block). Deleting row 6 and column 6 leaves the 5×5 matrix

$$A_5 = \begin{pmatrix} X_1 & 0 & 0 & a & 0 \\ -b & X_2 & 0 & -a & 0 \\ 0 & -\sigma & X_3 & 0 & 0 \\ 0 & 0 & -\gamma_L & X_4 & 0 \\ 0 & 0 & -\theta & -\theta_I & X_5 \end{pmatrix}. \tag{21}$$

Column 5 has the single nonzero entry X_5 (row 5), so $\det A_5 = X_5 \det A_4$, where

$$A_4 = \begin{pmatrix} X_1 & 0 & 0 & a \\ -b & X_2 & 0 & -a \\ 0 & -\sigma & X_3 & 0 \\ 0 & 0 & -\gamma_L & X_4 \end{pmatrix}. \tag{22}$$

Expanding A_4 along its first column,

$$\begin{aligned} \det A_4 &= X_1 \det \begin{pmatrix} X_2 & 0 & -a \\ -\sigma & X_3 & 0 \\ 0 & -\gamma_L & X_4 \end{pmatrix} + b \det \begin{pmatrix} 0 & 0 & a \\ -\sigma & X_3 & 0 \\ 0 & -\gamma_L & X_4 \end{pmatrix} \\ &= X_1 \big(X_2 X_3 X_4 - a\sigma\gamma_L \big) + b(a\sigma\gamma_L) \\ &= X_1 X_2 X_3 X_4 - a\sigma\gamma_L (X_1 - b). \end{aligned} \tag{23}$$

Since $X_1 - b = (\lambda + b + \mu) - b = \lambda + \mu$, this gives

$$\det A_4 = X_1 X_2 X_3 X_4 - a\sigma\gamma_L(\lambda + \mu) =: \det N_1, \tag{24}$$

so that expression is *confirmed* once N_1 is understood precisely as the 4×4 matrix A_4 in (22). Consequently

$$C_{66} = \det A_5 = X_5 \det N_1. \tag{25}$$

Step 3 (The M_{16} minor: the (E,L,I,H,R) block). Deleting row 1 and column 6 leaves the 5×5 matrix (rows 2–6, columns 1–5)

$$B_5 = \begin{pmatrix} -b & X_2 & 0 & -a & 0 \\ 0 & -\sigma & X_3 & 0 & 0 \\ 0 & 0 & -\gamma_L & X_4 & 0 \\ 0 & 0 & -\theta & -\theta_I & X_5 \\ 0 & 0 & -\rho_L & -\gamma_I & -\rho_H \end{pmatrix}. \tag{26}$$

Column 1 has the single nonzero entry $-b$ (row 1), so $\det B_5 = -b\det C_4$ with

$$C_4 = \begin{pmatrix} -\sigma & X_3 & 0 & 0 \\ 0 & -\gamma_L & X_4 & 0 \\ 0 & -\theta & -\theta_I & X_5 \\ 0 & -\rho_L & -\gamma_I & -\rho_H \end{pmatrix}. \tag{27}$$

Column 1 of C_4 has the single nonzero entry $-\sigma$ (row 1), so $\det C_4 = -\sigma\det D_3$, with

$$D_3 = \begin{pmatrix} -\gamma_L & X_4 & 0 \\ -\theta & -\theta_I & X_5 \\ -\rho_L & -\gamma_I & -\rho_H \end{pmatrix}. \tag{28}$$

Expanding D_3 along its first row,

$$\begin{aligned} \det D_3 &= -\gamma_L\big(\theta_I\rho_H + X_5\gamma_I\big) - X_4\big(\theta\rho_H + X_5\rho_L\big) \\ &= -\Big[\gamma_L(\theta_I\rho_H + X_5\gamma_I) + X_4(\theta\rho_H + X_5\rho_L)\Big]. \end{aligned} \tag{29}$$

Collecting the three nested factors, $\det B_5 = -b\det C_4 = -b(-\sigma\det D_3) = b\sigma\det D_3$, so

$$\det B_5 = -b\sigma\Big[\gamma_L(\theta_I\rho_H + X_5\gamma_I) + X_4(\theta\rho_H + X_5\rho_L)\Big]. \tag{30}$$

Define

$$N_2 := \sigma\Big[\gamma_L(\theta_I\rho_H + X_5\gamma_I) + X_4(\theta\rho_H + X_5\rho_L)\Big], \tag{31}$$

so that $\det B_5 = -bN_2$ (note N_2 is a *scalar expression*, not itself a determinant of a stated matrix). Then

$$C_{16} = (-1)^7\det B_5 = -\det B_5 = bN_2. \tag{32}$$

Step 4 (Assembling $P(\lambda)$). Substituting (25) and (32) into (20),

$$P(\lambda) = (-\phi)(bN_2) + X_6\big(X_5\det N_1\big) = X_5X_6\det N_1 - \phi bN_2. \tag{33}$$

Writing $\det N_1$ and N_2 out in full via (24) and (31) gives the explicit characteristic polynomial

$$P(\lambda) = X_5X_6\Big[X_1X_2X_3X_4 - a\sigma\gamma_L(\lambda+\mu)\Big] - \phi b\sigma\Big[\gamma_L(\theta_I\rho_H + X_5\gamma_I) + X_4(\theta\rho_H + X_5\rho_L)\Big] = 0, \tag{34}$$

this completes a term-by-term rederivation directly from J^{**} in (17), and confirms that the final expression (34) is algebraically correct; the correction made here relative to the original presentation is purely at the level of precisely defining N_1 (the 4×4 matrix in (22)) and N_2 (the scalar expression in (31)).
Expanding (34) in powers of λ yields the monic degree-six polynomial

$$P(\lambda) = \lambda^6 + a_1\lambda^5 + a_2\lambda^4 + a_3\lambda^3 + a_4\lambda^2 + a_5\lambda + a_6, \tag{35}$$

whose six roots are the eigenvalues of J^{**}. Two coefficients are pinned down directly by the structure above and are used later in this subsection:

- $a_1 = -\operatorname{tr}(J^{**}) = (b+\mu) + (\sigma+\mu) + P_L + P_I + P_H + (\phi+\mu)$, obtained as minus the sum of the six diagonal entries of J^{**};
- $a_6 = P(0) = \det(J^{**} - 0\cdot I) = \det(J^{**})$, obtained by setting $\lambda = 0$ (equivalently $X_i \to X_i(0)$) in (34).

The remaining coefficients $a_2,\ldots,a_5$ follow by collecting the corresponding powers of λ in (34); because (34) is fully explicit, this is a routine (if lengthy) symbolic expansion and is not reproduced term-by-term here.

3.6.3. Routh–Hurwitz Stability Criterion

The Routh–Hurwitz criterion for the monic polynomial (35) states that *all* roots have strictly negative real part *if and only if* all six leading principal minors $\Delta_1, \Delta_2, \ldots, \Delta_6$ of the associated Hurwitz matrix

$$H = \begin{pmatrix} a_1 & 1 & 0 & 0 & 0 & 0 \\ a_3 & a_2 & a_1 & 1 & 0 & 0 \\ a_5 & a_4 & a_3 & a_2 & a_1 & 1 \\ 0 & a_6 & a_5 & a_4 & a_3 & a_2 \\ 0 & 0 & 0 & a_6 & a_5 & a_4 \\ 0 & 0 & 0 & 0 & 0 & a_6 \end{pmatrix} \tag{36}$$

are strictly positive, i.e. $\Delta_1, \ldots, \Delta_6 > 0$.

It is well known (and follows directly from the Routh–Hurwitz array) that positivity of $a_1, \ldots, a_6$ is a *necessary* condition for $\Delta_1, \ldots, \Delta_6 > 0$: each a_k can be shown to appear, with a positive coefficient, along the boundary of the Hurwitz array, so that any $a_k \leq 0$ immediately forces at least one $\Delta_j \leq 0$ and hence instability. However, for a polynomial of degree $n \geq 3$ — and in particular for the degree-six polynomial (35) — positivity of $a_1, \ldots, a_6$ is *not sufficient* for Hurwitz stability: it guarantees none of the individual coefficient-based necessary conditions is violated, but it does not control the sign of the higher-order minors $\Delta_3, \Delta_4, \Delta_5, \Delta_6$, which involve products and differences of the a_k and can still be negative even when every $a_k > 0$. (This is in contrast to $n \leq 2$, where coefficient positivity is in fact both necessary and sufficient.) Accordingly, the earlier statement that coefficient positivity is "a sufficient (though not required) precondition" for stability is imprecise and is corrected here: *positivity of $a_1, \ldots, a_6$ is a necessary but generally insufficient precondition for local asymptotic stability of ∇^{**}*; the full set of conditions $\Delta_1, \ldots, \Delta_6 > 0$ must be verified to conclude stability rigorously.

3.6.4. Link to R_0 and the Scope of the Numerical Verification

Two structural observations connect (34) to the threshold quantity R_0 of Section 3.5.

1. Sign of the constant term. From (35), $a_6 = P(0) = \det(J^{**})$. Evaluating the X_i at $\lambda = 0$ in (34) and substituting the equilibrium relation $S^{**} = S^*/R_0$ (Section 3.3) shows that a_6 is proportional to $D(1 - 1/R_0)$, with $D > 0$ as defined in Eq. (5). Hence

$$a_6 > 0 \iff R_0 > 1, \tag{37}$$

the same threshold condition that guarantees ∇^{**} exists as a biologically feasible (strictly positive) equilibrium in the first place. By the necessity argument above, $R_0 > 1$ is therefore *necessary* for local asymptotic stability of ∇^{**} (since $a_6 \leq 0$ whenever $R_0 \leq 1$ forces instability), but — consistent with the corrected statement in Section 3.6.3 — $R_0 > 1$ alone does *not* establish sufficiency: it does not by itself guarantee $\Delta_1, \ldots, \Delta_6 > 0$.

2. Trace of J^{**}. $a_1 = -\operatorname{tr}(J^{**}) = (b+\mu) + (\sigma+\mu) + P_L + P_I + P_H + (\phi+\mu)$ is a sum of strictly positive terms, so $a_1 > 0$ unconditionally whenever ∇^{**} is a biologically meaningful (positive-parameter) equilibrium. This rules out the possibility of all six eigenvalues having positive real part but, per Section 3.6.3, is only one of the six necessary conditions and does not by itself establish stability.

Scope of the numerical check

Substituting the parameter values of Table 2 (for which $R_0 \approx 2.975$) together with the corresponding equilibrium quantities S^{**}, I^{**} (via Eqs. (4)–(6)) into J^{**} and evaluating the eigenvalues numerically confirms that all six eigenvalues have strictly negative real part *for this specific parameter set*. This is consistent with, and lends numerical support to, the qualitative convergence of the simulated trajectories in Figure 2 toward a positive steady state. It should be stressed, however, that this single evaluation verifies local asymptotic stability only at the one parameter point of Table 2; it does *not* constitute a proof that ∇^{**} is locally asymptotically stable for every parameter combination satisfying $R_0 > 1$. A general stability statement of that kind would require either

- an analytical demonstration that $\Delta_1, \ldots, \Delta_6 > 0$ hold identically whenever $R_0 > 1$, expressed directly in terms of the model parameters (a nontrivial symbolic Routh–Hurwitz analysis for a degree-six polynomial), or
- a systematic parameter-dependent numerical study — e.g. a Latin-hypercube or grid-based sweep over biologically plausible ranges of $\beta, \sigma, \gamma_L, \theta, \theta_I, \gamma_I, \rho_L, \rho_H, \delta_1, \delta_2, \phi, \mu$ with R_0 recomputed at each sample — together with a report of the fraction of sampled points for which all $\Delta_k > 0$, to build empirical (rather than pointwise) evidence for stability throughout the endemic region $R_0 > 1$.

In the absence of either, the stability conclusion of this subsection is stated more conservatively as: *the endemic equilibrium ∇^{**} is locally asymptotically stable for the estimated parameter regime of Table 2 ($R_0 \approx 3.185$)*, while the necessary condition $a_6 > 0 \iff R_0 > 1$ established above is the only property shown here to hold generically across the whole endemic parameter region. Establishing sufficiency of $R_0 > 1$ for stability in general is left as a direction for future analytical or parameter-sweep work, alongside the extensions already noted in Section 8 (spatial heterogeneity, age structure, stochastic effects, optimal control).

4. Modified Patankar-Runge-Kutta Schemes

Unlike classical higher-order general linear methods, which may violate essential qualitative properties of dynamical systems, the Modified Patankar-Runge-Kutta (MPRK) schemes are designed to be *unconditionally positivity-preserving* [18]. This property is particularly important in epidemiological modeling, where all state variables represent population classes and must remain nonnegative for biological consistency. Since all models considered in this study consist exclusively of nonnegative compartments, the MPRK framework is well suited for their numerical integration. The key idea underlying MPRK methods is the reformulation of a system of ordinary differential equations (ODEs) into a *production-destruction-rest* (PDR) form, which explicitly separates gain and loss mechanisms and allows positivity to be enforced at the discrete level [19].

Following [20], consider a general system of ODEs written in PDR form as

$$\frac{dc_i}{dt} = \sum_{j=1}^{N} p_{ij}(\underline{c}) - \left(r_i^D(\underline{c}) + \sum_{j=1}^{N} d_{ij}(\underline{c}) \right) c_i + r_i^p(\underline{c}), \quad i = 1,\ldots,N, \tag{38}$$

where $c_i(t)$ denotes the i-th state variable, $p_{ij}(c)$ represents the production of c_i from c_j, $d_{ij}(c)$ denotes destruction due to interactions with other compartments, $r_i^D(\underline{c})$ is a linear destruction *rate* (not a flux – it is multiplied by c_i by the equation itself), and $r_i^p(\underline{c})$ is an external production (rest) term. Applying an s-stage MPRK discretization to this system yields the internal stage values

$$c_i^{(k)} = c_i^n + \Delta t \sum_{\nu=1}^{k-1} a_{k\nu} \left(\sum_{j=1}^{N} p_{ij}\left(c^{(\nu)}\right) \frac{c_j^{(k)}}{\pi_j^{(k)}} - \left(r_i^D\left(c^{(\nu)}\right) + \sum_{j=1}^{N} d_{ij}\left(c^{(\nu)}\right) \right) \frac{c_i^{(k)}}{\pi_i^{(k)}} \right) + \Delta t \sum_{\nu=1}^{k-1} a_{k\nu} r_i^p\left(\underline{c}^{(\nu)}\right), \tag{39}$$

for $k = 1,\ldots,s$, and the final update

$$c_i^{n+1} = c_i^n + \Delta t \sum_{k=1}^{s} b_k \left(\sum_{j=1}^{N} p_{ij}\left(\underline{c}^{(k)}\right) \frac{c_j^{n+1}}{\sigma_j} - \left(r_i^D\left(\underline{c}^{(k)}\right) + \sum_{j=1}^{N} d_{ij}\left(\underline{c}^{(k)}\right) \right) \frac{c_i^{n+1}}{\sigma_i} \right) + \Delta t \sum_{k=1}^{s} b_k r_i^p\left(\underline{c}^{(k)}\right). \tag{40}$$

Here, $\pi_i^{(k)}$ and σ_i are the Patankar weighted denominators (PWDs), defined such that

$$\pi_i^{(k)} = \pi_i^{(n)}\left(\underline{c}^n, \underline{c}^{(1)}, \ldots, \underline{c}^{(k-1)}\right) > 0 \quad \text{for } \underline{c}^n > 0,$$

$$\sigma_i = \sigma_i\left(\underline{c}^n, \underline{c}^{(1)}, \ldots, \underline{c}^{(s)}\right) > 0 \quad \text{for } \underline{c}^n > 0.$$

These denominators play a central role in guaranteeing unconditional positivity of the numerical solution by ensuring that all production and destruction terms are properly weighted with strictly positive quantities.

To recover the first-order MPRK method, known as the Modified Patankar-Euler (MPE) scheme, we set $s = 1$. In this case, there are no internal stages, and equation (39) reduces trivially to

$$c_i^{(1)} = c_i^n.$$

Consequently, the intermediate denominators $\pi_i^{(k)}$ are not required. By choosing the final Patankar denominators as $\sigma_i = c_i^n$, the update formula (40) simplifies to

$$c_i^{n+1} = c_i^n + \Delta t \sum_{j=1}^{N} p_{ij}(\underline{c}^n) \frac{c_j^{n+1}}{c_j^n} - \Delta t \left(r_i^D(\underline{c}^n) + \sum_{j=1}^{N} d_{ij}(\underline{c}^n) \right) \frac{c_i^{n+1}}{c_i^n} + \Delta t\, r_i^p(c^n), \tag{41}$$

which defines the Modified Patankar-Euler scheme [21]. This method is first-order accurate in time and, importantly, preserves nonnegativity of all solution components for arbitrary time step sizes. As such, it provides a reliable baseline integrator for epidemiological models, while higher-order MPRK schemes extend these desirable properties to more accurate time discretizations.

We now extend the above analysis of the Modified Patankar-Euler (MPE) scheme (corresponding to $s = 1$) to a second-order Modified Patankar-Runge-Kutta scheme with two stages ($s = 2$). This extension follows the same production-destruction framework and preserves the structural properties established for the MPE scheme.

In the case of the MPRK scheme, it is based on a two-stage, second-order explicit Runge-Kutta method (Heun's method) with Butcher tableau

$$\begin{array}{c|cc} 0 & 0 & 0 \\ 1 & 1 & 0 \\ \hline & \frac{1}{2} & \frac{1}{2} \end{array}$$

Thus, for $s = 2$, we have

$$a_{21} = 1, \quad b_1 = \frac{1}{2}, \quad b_2 = \frac{1}{2}, \quad c_1 = 0, \quad c_2 = 1.$$

As in the first-order case,

$$c_i^{(1)} = c_i^n.$$

Using the general MPRK formulation (39) with $a_{21} = 1$, the second stage reads

$$c_i^{(2)} = c_i^n + \Delta t \left[\sum_{j=1}^{N} p_{ij}\left(\underline{c}^{(1)}\right) \frac{c_j^{(2)}}{\pi_j^{(2)}} - \left(r_i^D\left(\underline{c}^{(1)}\right) + \sum_{j=1}^{N} d_{ij}\left(\underline{c}^{(1)}\right) \right) \frac{c_i^{(2)}}{\pi_i^{(2)}} \right] + \Delta t\, r_i^p\left(\underline{c}^{(1)}\right). \tag{42}$$

Since the first stage of this (explicit, $c_1 = 0$) tableau is trivial, $\underline{c}^{(1)} = \underline{c}^n$, the only admissible choice consistent with $\pi_i^{(2)} = \pi_i^{(2)}(\underline{c}^n, \underline{c}^{(1)}) > 0$ is

$$\pi_i^{(2)} = c_i^{(1)} = c_i^n. \tag{43}$$

Solving (42) for $c_i^{(2)}$ gives

$$c_i^{(2)} = \frac{c_i^n + \Delta t\, r_i^p\left(\underline{c}^{(1)}\right) + \Delta t \sum_{j=1}^N p_{ij}\left(\underline{c}^{(1)}\right)\dfrac{c_j^{(2)}}{c_j^n}}{1 + \dfrac{\Delta t}{c_i^n}\left(r_i^D\left(\underline{c}^{(1)}\right) + \sum_{j=1}^N d_{ij}\left(\underline{c}^{(1)}\right)\right)}. \tag{44}$$

For the final update, the general formula (40) requires $\sigma_i = \sigma_i(\underline{c}^n, \underline{c}^{(1)}, \underline{c}^{(2)}) > 0$. Following the same logic as Burchard et al.'s original second-order scheme — where the corrector is normalized by the nontrivial intermediate stage rather than by the old time level — the correct (order-consistent) choice for this Heun-based MPRK22 is

$$\sigma_i = c_i^{(2)}, \tag{45}$$

not $\sigma_i = c_i^n$. With this choice,

$$\begin{aligned} c_i^{n+1} = c_i^n + \frac{\Delta t}{2}\sum_{j=1}^N \left(p_{ij}(\underline{c}^{(1)}) + p_{ij}(\underline{c}^{(2)})\right)\frac{c_j^{n+1}}{c_j^{(2)}} - \frac{\Delta t}{2}\left(r_i^D\left(\underline{c}^{(1)}\right) + r_i^D\left(\underline{c}^{(2)}\right) + \sum_{j=1}^N \left(d_{ij}(\underline{c}^{(1)}) + d_{ij}(\underline{c}^{(2)})\right)\right)\frac{c_i^{n+1}}{c_i^{(2)}} \\ + \frac{\Delta t}{2}\left(r_i^p(\underline{c}^{(1)}) + r_i^p(\underline{c}^{(2)})\right). \end{aligned} \tag{46}$$

Rearranging and making c_i^{n+1} the subject,

$$c_i^{n+1} = \frac{c_i^n + \dfrac{\Delta t}{2}\left(r_i^p(\underline{c}^{(1)}) + r_i^p(\underline{c}^{(2)})\right) + \dfrac{\Delta t}{2}\displaystyle\sum_{j=1}^N \left(p_{ij}(\underline{c}^{(1)}) + p_{ij}(\underline{c}^{(2)})\right)\frac{c_j^{n+1}}{c_j^{(2)}}}{1 + \dfrac{\Delta t}{2c_i^{(2)}}\left(r_i^D\left(\underline{c}^{(1)}\right) + r_i^D\left(\underline{c}^{(2)}\right) + \displaystyle\sum_{j=1}^N \left(d_{ij}(\underline{c}^{(1)}) + d_{ij}(\underline{c}^{(2)})\right)\right)}. \tag{47}$$

For the purpose of this study, the second-order MPRK method with the denominator choice (45) was adopted for the numerical simulation.

5. Production-Destruction-Rest Decomposition of the COVID-19 Model

We now cast the six-compartment model, system (1), into the PDR form (38) required by the MPRK framework, with compartments indexed as $(c_1, \ldots, c_6) = (S, E, L, I, H, R)$.

5.1. Production Terms

Every inter-compartmental transition in system (1) is a linear or bilinear transfer from a source compartment to a destination compartment, so it is captured entirely by the production terms $p_{ij}(\underline{c})$ (production of c_i from c_j); no separate bilinear destruction terms $d_{ij}(\underline{c})$ are required for this model. The nonzero production terms are:

$$\begin{aligned} &p_{16}(\underline{c}) = \phi R, \qquad p_{21}(\underline{c}) = \beta IS, \qquad p_{32}(\underline{c}) = \sigma E, \\ &p_{43}(\underline{c}) = \gamma_L L, \qquad p_{53}(\underline{c}) = \theta L, \qquad p_{54}(\underline{c}) = \theta_I I, \\ &p_{64}(\underline{c}) = \gamma_I I, \qquad p_{65}(\underline{c}) = \rho_H H, \qquad p_{63}(\underline{c}) = \rho_L L. \end{aligned}$$

5.2. Rest Terms

The rest terms capture recruitment into the system (external production) and linear natural/disease-induced mortality (destruction *rates*, per the definition of r_i^D in equation (38)):

$$\begin{aligned} &r_1^p = \Lambda, \qquad r_2^p = r_3^p = r_4^p = r_5^p = r_6^p = 0, \\ &r_1^D = \mu, \quad r_2^D = \mu, \quad r_3^D = \mu, \quad r_4^D = \mu + \delta_1, \quad r_5^D = \mu + \delta_2, \quad r_6^D = \mu. \end{aligned}$$

5.3. Matrix Representation

The production matrix $P(\underline{c})$ for model (1) can be written explicitly as:

$$P(\underline{c}) = \begin{pmatrix} 0 & 0 & 0 & 0 & 0 & \phi R \\ \beta IS & 0 & 0 & 0 & 0 & 0 \\ 0 & \sigma E & 0 & 0 & 0 & 0 \\ 0 & 0 & \gamma_L L & 0 & 0 & 0 \\ 0 & 0 & \theta L & \theta_I I & 0 & 0 \\ 0 & 0 & \rho_L L & \gamma_I I & \rho_H H & 0 \end{pmatrix} \tag{48}$$

and the production-destruction vectors corresponding to the rest terms are:

$$r^p(\underline{c}) = \begin{pmatrix} \Lambda \\ 0 \\ 0 \\ 0 \\ 0 \\ 0 \end{pmatrix} \qquad r^D(\underline{c}) = \begin{pmatrix} \mu \\ \mu \\ \mu \\ \mu + \delta_1 \\ \mu + \delta_2 \\ \mu \end{pmatrix} \tag{49}$$

6. Application of the MPRK1 and MPRK22 Schemes to the COVID-19 Model

Having identified the model's production, rest, and destruction terms in Section 5 (with $d_{ij}(\underline{c}) \equiv 0$ for all i, j), we now substitute them into the general MPRK1 and MPRK22 formulas of the previous section to obtain the concrete scheme that is actually solved at each time step.

6.1. MPRK1 (MPE (first-order)) applied to the model

Substituting equations (48) and (49), with $d_{ij} \equiv 0$, into the general MPE update (41) gives the linear system

$$-\Delta t \sum_{j=1}^{6} p_{ij}(c^n) \frac{c_j^{(n+1)}}{c_j^n} + \left(1 + \frac{\Delta t\, r_i^D}{c_i^n}\right) c_i^{(n+1)} = c_i^n + \Delta t\, r_i^p \tag{50}$$

where

$$m_{ii} = 1 + \frac{\Delta t\, r_i^D}{c_i^n}, \qquad m_{ij} = -\frac{\Delta t\, p_{ij}(c^n)}{c_j^n}, \quad i \neq j. \tag{51}$$

Since r_i^D is constant in this model (it does not depend on $\underline{c}$), m_{ii} takes the explicit values $m_{11} = m_{22} = m_{33} = m_{66} = 1 + \Delta t\, \mu / c_i^n$, $m_{44} = 1 + \Delta t(\mu + \delta_1)/I^n$, and $m_{55} = 1 + \Delta t(\mu + \delta_2)/H^n$, while the nine nonzero off-diagonal entries m_{ij} follow directly from the nine nonzero production terms listed in Section 5.

6.2. MPRK22 (second-order) applied to the model

For the two-stage MPRK22 scheme, we adopt $\pi_j^{(2)} = c_j^{(1)} = c_j^n$ for the intermediate stage, and $\sigma_j = c_j^{(2)}$ — i.e. the *second*-stage values, not c_j^n — for the final update, consistent with (44)–(47). Substituting the model's terms (with $d_{ij} \equiv 0$) gives the stage-2 linear system

$$c_i^{(2)} \left[1 + \frac{\Delta t}{c_i^n} r_i^D\right] - \Delta t \sum_{j=1}^{6} p_{ij}(\underline{c}^{(1)}) \frac{c_j^{(2)}}{c_j^n} = c_i^n + \Delta t\, r_i^p\left(\underline{c}^{(1)}\right), \tag{52}$$

where $r_1^p(\underline{c}^{(1)}) = \Lambda$ and $r_i^p(\underline{c}^{(1)}) = 0$ for $i = 2, \ldots, 6$. Once $\underline{c}^{(2)}$ has been obtained, the final-update linear system reads

$$-\frac{\Delta t}{2} \sum_{j=1}^{6} \left(p_{ij}(\underline{c}^{(1)}) + p_{ij}(\underline{c}^{(2)})\right) \frac{c_j^{n+1}}{c_j^{(2)}} + \left(1 + \frac{\Delta t}{2c_i^{(2)}} \left(r_i^D\left(\underline{c}^{(1)}\right) + r_i^D\left(\underline{c}^{(2)}\right)\right)\right) c_i^{n+1} = c_i^n + \frac{\Delta t}{2} \left(r_i^p(\underline{c}^{(1)}) + r_i^p(\underline{c}^{(2)})\right), \tag{53}$$

with coefficients

$$m_{ii}^{(2)} = 1 + \frac{\Delta t}{2c_i^{(2)}} \left(r_i^D\left(\underline{c}^{(1)}\right) + r_i^D\left(\underline{c}^{(2)}\right)\right) = 1 + \frac{\Delta t\, r_i^D}{c_i^{(2)}}, \qquad m_{ij}^{(2)} = -\frac{\Delta t}{2c_j^{(2)}} \left(p_{ij}(\underline{c}^{(1)}) + p_{ij}(\underline{c}^{(2)})\right), \quad i \neq j, \tag{54}$$

the simplification of $m_{ii}^{(2)}$ following from $r_i^D(\underline{c}^{(1)}) = r_i^D(\underline{c}^{(2)}) = r_i^D$, since r_i^D is constant for this model.

Denote by $\mathbf{M}^{(1)} = (m_{ij}^{(1)})$ the matrix of the stage-2 system (52), with $m_{ii}^{(1)} = 1 + \Delta t\, r_i^D / c_i^n$ and $m_{ij}^{(1)} = -\Delta t\, p_{ij}(\underline{c}^{(1)})/c_j^n$, and by $\mathbf{M}^{(2)} = (m_{ij}^{(2)})$ the matrix of the final system (53) in (54). Both matrices share the same sparsity pattern — one equation per compartment, with the nine nonzero couplings dictated by the production matrix (48) — but they are *not* numerically identical: $\mathbf{M}^{(1)}$ is normalized by the previous-step values c_j^n, whereas $\mathbf{M}^{(2)}$ is normalized by the second-stage values $c_j^{(2)}$. Writing $\mathbf{M}^{(1)}\mathbf{c}^{(2)} = \mathbf{b}^{(1)}$ for equation (52) and $\mathbf{M}^{(2)}\mathbf{c}^{n+1} = \mathbf{b}^{(2)}$ for equation (53), both systems take the general matrix form

$$\mathbf{M}^{(k)}\,\mathbf{c} = \mathbf{b}^{(k)}, \qquad k = 1, 2, \tag{55}$$

where each $\mathbf{M}^{(k)} = (m_{ij}^{(k)}) \in \mathbb{R}^{6\times 6}$ is lower-triangular up to the single entry $m_{16}^{(k)}$ (coupling S back to R through waning immunity), and is solved once per stage to advance the solution from t_n to t_{n+1}.

7. Numerical Simulation

This section focuses on the numerical simulation of the COVID-19 model. The Table 2 contains the parameter values used in this study for the simulation of the model; some adopted from literature and the others estimated using synthetic data.Table 3 on the other had, represent the initial values chosen for the state variables. All numerical methods were implemented in Python.

Table 2: Parameter values used in the COVID-19 model

Parameter	Description	Value	Status
Λ	Recruitment rate	1300	Assumed
β	Transmission coefficient	0.000000027	Assumed
μ	Natural mortality rate	0.000042578	[22]
ϕ	Loss of immunity rate	0.011	[23]
σ	Exposed-to-latent progression rate	0.13	[23]
ρ_L	Recovery rate from latent class	0.10	Assumed
θ	Hospitalization rate from latent class	0.03	Assumed
γ_L	Latent-to-infectious progression rate	0.13978	[23]
θ_I	Hospitalization rate from infectious class	0.086	Assumed
γ_I	Recovery rate from infectious class	0.03	Assumed
ρ_H	Recovery rate from hospitalized class	0.05	Assumed
δ_1	Disease-induced mortality rate in infectious class	0.018	[23]
δ_2	Disease-induced mortality rate in hospitalized class	0.018	[23]

Table 3: Initial conditions for the state variables

Compartment	Initial Value
$S(0)$	32,999,640
$E(0)$	200
$L(0)$	100
$I(0)$	50
$H(0)$	10
$R(0)$	0

The Figure 2 shows a single-wave epidemic curve from a SELIHR model: susceptibles stay flat until about t = 75, then drop sharply as exposed, latent, infected, and hospitalized cases rise and peak in sequence between roughly t = 100–155, each compartment peaking a bit later and lower than the last. Recovered cases climb steadily from around t = 100 and plateau near 21–22 million by t = 200, marking the end of the outbreak as susceptibles are depleted.

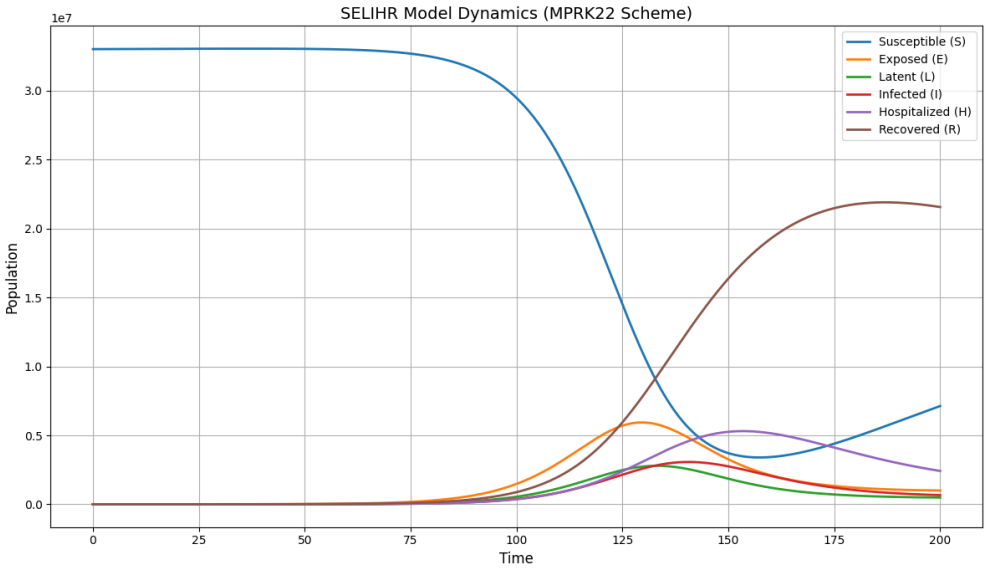
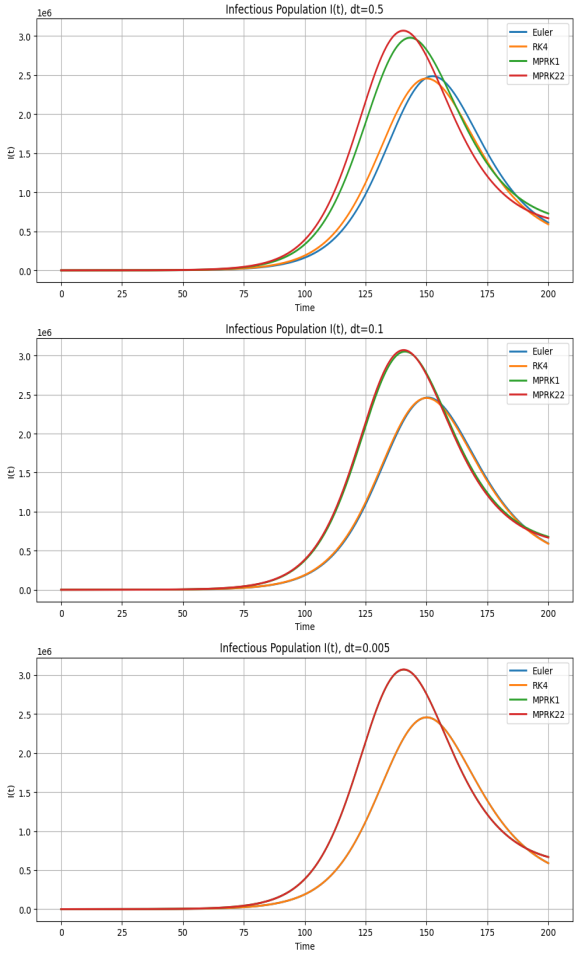


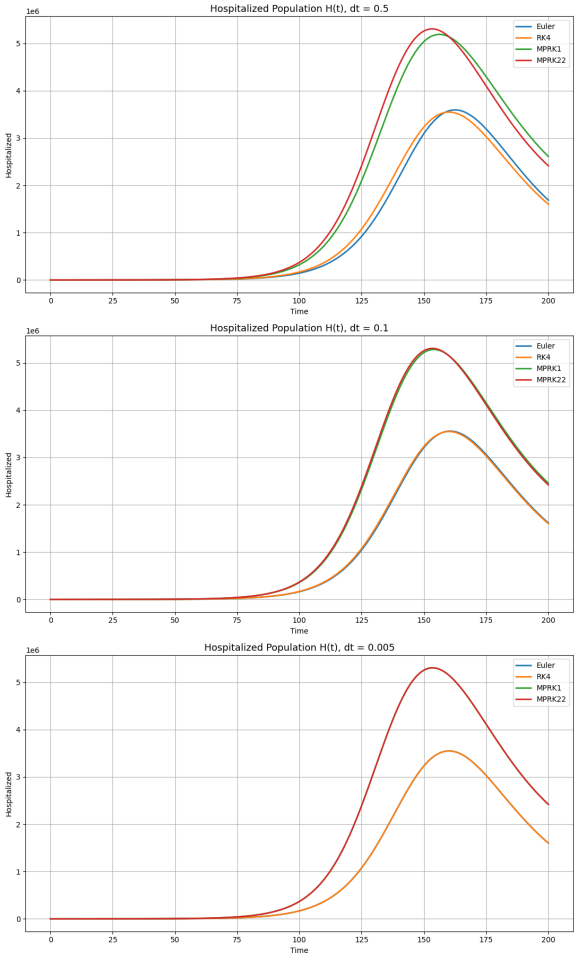
Figure 2: Outcome of COVID-19 Model Using MPRK22 Scheme [24]

Throughout the simulation, all trajectories remain smooth, strictly nonnegative, and free of numerical oscillations, confirming that the MPRK22 scheme preserves positivity and boundedness even in the presence of strong nonlinear interactions among compartments. These results demonstrate that the method accurately captures the timing and magnitude of epidemic peaks while remaining stable, making it particularly well suited for long-term simulations and policy-relevant scenario analysis in COVID-19 modeling.

To assess the robustness and comparative performance of the proposed MPRK22 scheme against traditional numerical methods, simulations were first conducted using the initial conditions listed in Table 3 together with the parameter values in Tables 2. Under this baseline setting, the MPRK22 method and the competing schemes were applied to solve the model, with focus on only the infected and hospitalized compartments, and at varying time step $\Delta t = 0.5$, 0.1, and 0.005. These simulations provide a direct comparison of the methods under epidemiologically realistic initial conditions at varied time steps as shown in Figure 3a and Figure 3b.



(a) Infectious compartment



(b) Hospitalized compartment

Figure 3: Comparison of the effects of varying time step sizes ($\Delta t = 0.5$, 0.1, 0.005) on the Infectious and Hospitalized compartments, for the Euler, RK4, MPRK1, and MPRK22 schemes[24]

The Figure 3a compares I(t) across Euler, RK4, MPRK1, and MPRK22 at three step sizes (dt = 0.5, 0.1, 0.005). MPRK1 and MPRK22 stay stable and closely matched at all step sizes, peaking near 3.0–3.1 million around t = 140. Euler starts off underestimating the peak at large dt but converges toward the MPRK curves as dt shrinks. RK4, however, consistently converges to a lower, later peak (2.5 million near t = 150) even at the finest step size, pointing to a persistent discrepancy from the other methods on this stiff system. Similarly, the Figure 3b compares H(t) across Euler, RK4, MPRK1, and MPRK22 at three step sizes (dt = 0.5, 0.1, 0.005). MPRK1 and MPRK22 are stable across all step sizes, peaking near 5.2–5.3 million around t = 150–155. Euler and RK4 start out underestimating the peak (3.5–3.6 million, later timing) at large dt, and converge to each other as dt shrinks, but even at the finest step size they remain well below the MPRK peak. This persistent gap suggests a real difference between the two families of schemes on this stiff system, not just a step-size artifact.

Computational Procedure

The following generalized steps were used to determine the computational efficiency of the numerical schemes.

Step 1: Problem setup. Let the governing initial value problem be given by

$$\frac{dy}{dt} = f(t,y), \qquad y(t_0) = y_0,$$

and let $y_{\text{ref}}(t)$ denote a reference solution obtained at high resolution. Define the set of numerical schemes

$$\mathscr{M} = \{\text{Euler},\ \text{RK4},\ \text{MPRK1},\ \text{MPRK22}\},$$

and the set of time steps

$$\Delta t \in \{0.05,\ 0.10,\ 0.25,\ 0.50,\ 1,\ 2,\ 4,\ 8,\ 16\}.$$

Step 2: Numerical integration. For each scheme $M \in \mathscr{M}$ and each time step Δt_k, the solution is advanced according to

$$y_{n+1} = M(y_n, \Delta t_k), \qquad n = 0, 1, \ldots, N_{\text{steps}} - 1, \quad N_{\text{steps}} = \left\lceil \frac{T_{\text{final}} - t_0}{\Delta t_k} \right\rceil,$$

where $M(\cdot,\cdot)$ denotes the discrete update rule associated with Euler, RK4, MPRK1, or MPRK22.

Step 3: Runtime measurement. The computational cost of each simulation is recorded as

$$T(M, \Delta t_k) = t_{\text{end}} - t_{\text{start}},$$

where t_{start} and t_{end} denote the wall-clock times immediately before and after integration.

Step 4: Relative error computation. The accuracy of each scheme is quantified by the relative error at the final time,

$$E(M, \Delta t_k) = \frac{\left\| y_{N_{\text{steps}}} - y_{\text{ref}}(T_{\text{final}}) \right\|}{\| y_{\text{ref}}(T_{\text{final}}) \|}.$$

Step 5: Positivity check. For each compartment i and time level n, the number of negative values produced by the scheme is counted as

$$\mathscr{N}(M, \Delta t_k) = \sum_{n=0}^{N_{\text{steps}}} \sum_i \mathbb{1}\left[y_n^{(i)} < 0 \right],$$

where $\mathbb{1}[\cdot]$ is the indicator function.

Step 6: Stability classification. Each simulation is classified as

$$S(M, \Delta t_k) = \begin{cases} \text{Stable}, & \text{if } y_n \text{ remains finite for all } n, \\ \text{Unstable}, & \text{if } y_n \to \infty \text{ or } y_n = \text{NaN for some } n. \end{cases}$$

Step 7: Observed convergence order. For each scheme, the observed order of convergence between consecutive step sizes Δt_k and Δt_{k+1} is estimated using

$$p(M) = \frac{\ln(E(M, \Delta t_{k+1}) / E(M, \Delta t_k))}{\ln(\Delta t_{k+1} / \Delta t_k)}.$$

Step 8: Summary statistics. For each scheme M, the overall performance is summarized by

$$E_{\min}(M) = \min_k E(M, \Delta t_k), \qquad E_{\max}(M) = \max_k E(M, \Delta t_k),$$

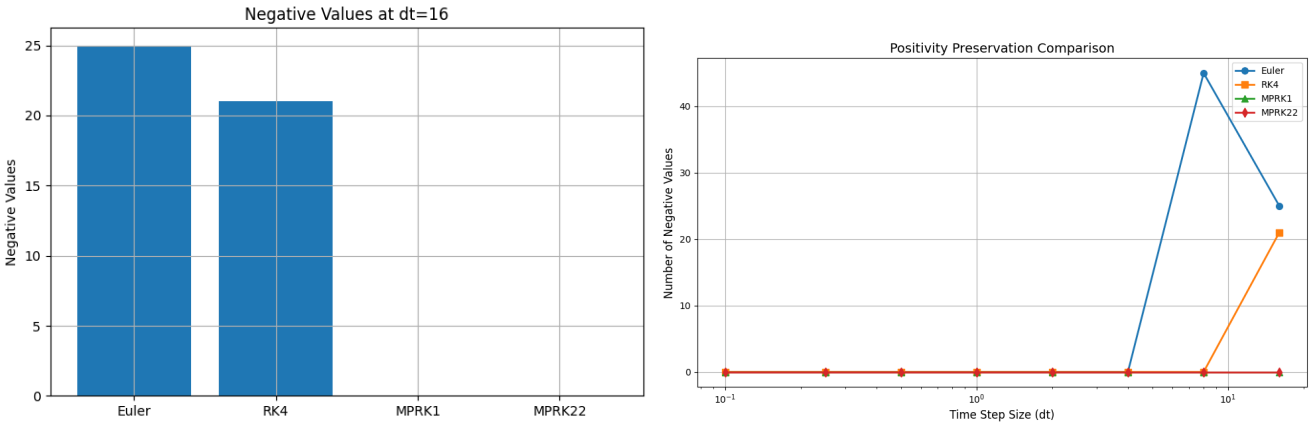
$$T_{\min}(M) = \min_k T(M, \Delta t_k), \qquad T_{\max}(M) = \max_k T(M, \Delta t_k),$$

$$\mathscr{N}_{\max}(M) = \max_k \mathscr{N}(M, \Delta t_k), \qquad S_{\text{overall}}(M) = \bigwedge_k S(M, \Delta t_k).$$

Step 9: Comparative analysis. The quantities $E(M, \Delta t_k)$, $T(M, \Delta t_k)$, $\mathscr{N}(M, \Delta t_k)$, and $S(M, \Delta t_k)$ are tabulated and plotted across schemes and step sizes to assess accuracy, computational cost, positivity preservation, and stability, respectively.

Table 4: Comparison of positivity preservation among the numerical methods for the SELIHR model.

Δt	**Euler**	**RK4**	**MPRK1**	**MPRK22**
0.10	0	0	**0**	**0**
0.25	0	0	**0**	**0**
0.50	0	0	**0**	**0**
1	0	0	**0**	**0**
2	0	0	**0**	**0**
4	0	0	**0**	**0**
8	45	0	**0**	**0**
16	25	21	**0**	**0**



(a) Negative Values against Schemes

(b) Negative Values against Time Step

Figure 4: Positivity Preservation Comparison of Euler, RK4, MPRK1, and MPRK22 schemes [24]

The Figure 4a reports the number of negative values produced by each numerical scheme when integrating the model with a large step size of dt = 16, serving as a direct test of positivity preservation under coarse time discretization, as can be seen in the data in Table 4. The classical Euler and RK4 methods generate 25 and 21 negative values, respectively, demonstrating that both schemes fail to preserve the non-negativity of the state variables at this step size. In contrast, the modified Patankar-Runge-Kutta schemes, MPRK1 and MPRK22, produce zero negative values, confirming their unconditional positivity-preserving property regardless of step size. This result highlights a key practical advantage of the MPRK schemes over standard explicit methods for stiff, positivity-constrained systems such as epidemiological compartment models, where large time steps are often desirable for computational efficiency but risk producing non-physical negative populations with conventional solvers. Additionally, the Figure 4b tracks the number of negative values from each scheme across step sizes from dt = 0.1 to 16 (log scale). All schemes stay positive up to dt = 4. Beyond that, Euler breaks down first, spiking to 45 negative values at dt = 8 and 25 at dt = 16, while RK4 holds up until dt = 16, where it produces 21 negative values. MPRK1 and MPRK22 stay at zero across the entire range, confirming they preserve positivity unconditionally, unlike the classical schemes which only do so below a step-size threshold.

This Figure 5 classifies each scheme as stable or unstable across $\Delta t = 0.1$ to 16. Euler, MPRK1, and MPRK22 stay stable throughout the whole range, even at $\Delta t = 16$, while RK4 holds up to $\Delta t = 8$ but flips to unstable at $\Delta t = 16$. Note that "stable" here just means the solution doesn't blow up; it's a separate question from positivity, so a scheme can be stable and still produce negative values, as seen earlier with Euler.

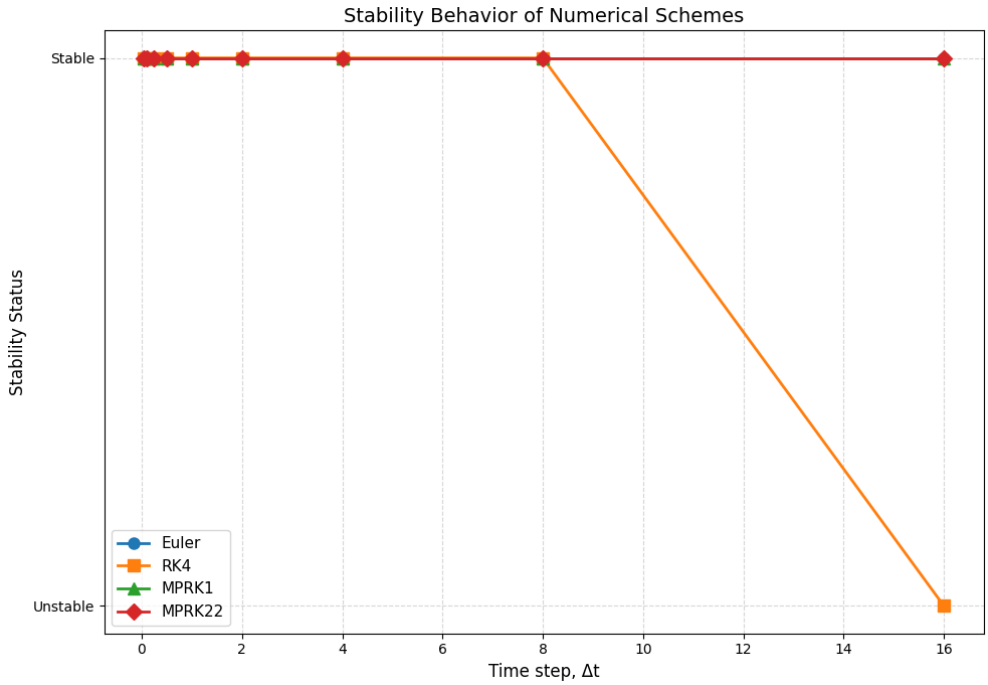
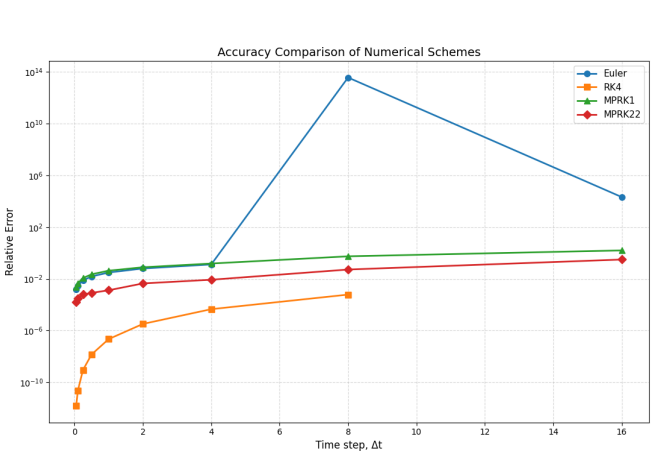
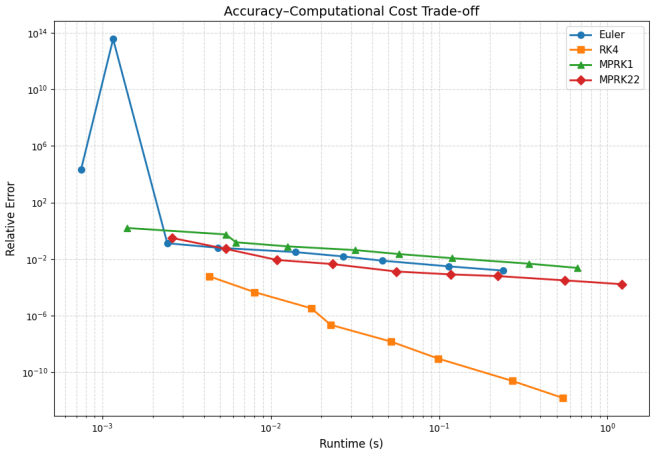


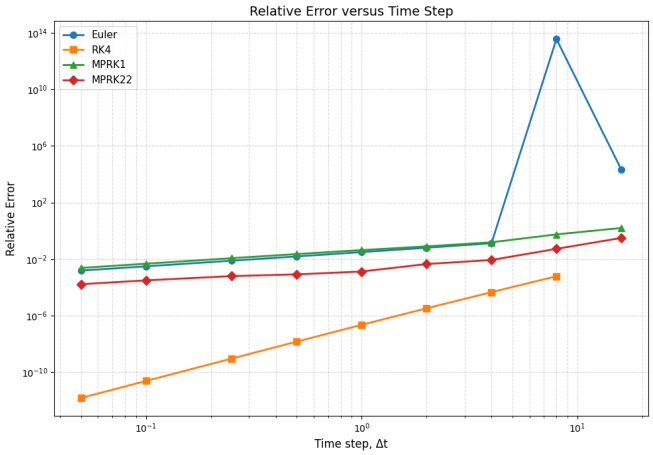
Figure 5: Stability behavavior of Euler, RK4, MPRK1, and MPRK22 schemes [24]



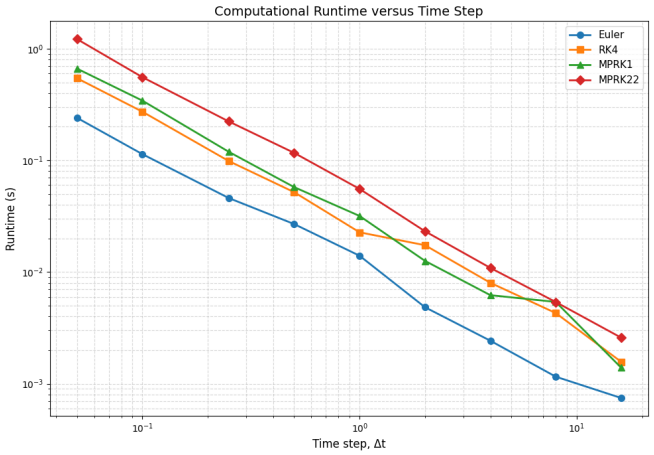
(a) Accuracy of Schemes



(b) Accuracy-Computational Cost Trade-off



(c) Relative Error vrs Time Step



(d) Runtime vrs Time Step

Figure 6: Computational Efficiency of the Schemes [24]

The Figure 6a compares relative error vs. step size ($\Delta t = 0.1$–16, log scale) for all four schemes. RK4 has the lowest error throughout, staying under 10^{-4} even at $\Delta t = 8$ (no data at $\Delta t = 16$, since it went unstable there). MPRK1 and MPRK22 show similar, gradually increasing error, staying in a moderate 10^{-2}–10^{1} range even at $\Delta t = 16$, stable and predictable degradation. Euler looks fine at small step sizes but spikes to 10^{14} error at $\Delta t = 8$, then drops to 10^{3} at $\Delta t = 16$; an erratic blow-up that lines up with the instability and negative values seen earlier. Overall, RK4 wins on accuracy when well-resolved, but MPRK schemes are far more robust at large step sizes.The Figure 6b plots relative error vs. runtime (log-log) for all four schemes, each point representing a different step size. RK4 gives the best accuracy per runtime overall, though it's missing points at the largest step sizes where it went unstable. MPRK1 and MPRK22 form smooth, closely-matched curves across the full runtime range (MPRK22 slightly more accurate than MPRK1), with no missing or erratic points; reflecting their unconditional stability. Euler is erratic at short runtimes (large step sizes), spiking to 10^{14} error before settling into a smoother trend at longer runtimes. The takeaway: Euler's apparent speed advantage at large step sizes is illusory since it's unreliable there, while the MPRK schemes offer a consistent, dependable trade-off across the board.

The Figure 6c plots relative error vs. Δt (log-log, from 0.05 to 16) to compare convergence rates. RK4 has the steepest slope (fourth-order convergence) and lowest error in the well-resolved range, but has no data at the largest step sizes where it went unstable. MPRK1 and MPRK22 show shallower, near-parallel slopes (lower convergence order), increasing smoothly and predictably all the way to $\Delta t = 16$, with MPRK22 slightly more accurate than MPRK1. Euler tracks similarly to the MPRK schemes at small Δt but then spikes sharply at $\Delta t = 8$ (10^{14} error) before dropping at $\Delta t = 16$; a clear instability signature. Overall: RK4 is most accurate when stable, but MPRK schemes trade some accuracy for reliable, predictable behavior across all tested step sizes. The Figure 6d also shows runtime vs. Δt (log-log) for all four schemes. Runtime decreases monotonically with larger step sizes for all methods, as expected. Euler is fastest at every step size, followed by RK4, while MPRK1 and MPRK22 cost more; with MPRK22 generally the most expensive, reflecting the extra overhead of its positivity-preserving corrections. At the largest step sizes ($\Delta t = 8, 16$), the curves converge and even cross, likely due to fixed overhead dominating as the number of steps shrinks. Overall: the MPRK schemes' stability and positivity guarantees come at a modest but consistent runtime cost compared to Euler and RK4.

8. Conclusion

The study analyzed a six-compartment COVID-19 model (system (1)) that reflects the real stages of infection: exposure, latency, active infectiousness, hospitalization, recovery, disease-induced death, and the eventual loss of immunity. It proved analytically that the model behaves the way an epidemic model should; solutions stay non-negative, the total population stays bounded, and there's a positively invariant region; so the model is both mathematically sound and epidemiologically sensible.

The system (1) has both an endemic and a disease-free equilibrium, according to the equilibrium analysis. The fundamental reproduction number for the parameter set was determined to be $R_0 \approx 3.185$ using the next-generation matrix approach. A value this high indicates that the disease-free condition is fragile and that the disease will spread rapidly if left unchecked. This highlights the need for treatments that reduce transmission, expedite hospitalization and isolation, or decrease the infectious period sufficiently to bring R_0 below 1.

On the numerical side, the system (1) was solved using the MPRK22 scheme after rewriting it in production–destruction–rest form. This reformulation let MPRK22 do what it's designed to do: preserve positivity and conservation properties automatically, without needing artificial fixes. Simulations showed that MPRK22 captures the timing and size of the epidemic peaks accurately, and stays stable over long simulation horizons.

The results of the MPRK22 scheme was compared against the classical Euler and RK4 methods, along with the first-order MPRK1 scheme, across a range of time-step sizes. At small steps, all four methods showed essentially the same result. But as the step size grows, cracks appear in the classical methods: Euler starts producing negative, and therefore biologically meaningless; population values once the step size reaches 8, and continues to do so at 16; RK4 holds up a little longer but also produces negative values at a step size of 16, and becomes fully unstable there too. MPRK1 and MPRK22, on the other hand, never produce a single negative value across the entire range we tested, and both remain numerically stable throughout; even at the largest step sizes where the classical methods break down.

Taken together, these findings show that the Modified Patankar–Runge–Kutta schemes, and MPRK22 in particular, are dependable tools for modeling COVID-19 and similar infectious diseases. Their ability to preserve positivity and stability even at large time steps makes them especially useful for long-term simulations, sensitivity analyses, and the kind of scenario planning that actually informs public health decisions; situations where you can't afford a model to hand you a negative number of sick people. Future work could extend this framework to account for spatial spread, age structure, randomness in transmission, or optimal control strategies, further widening the practical reach of MPRK-based methods in public health modeling.

Article Information

Funding: No external funding was received for this study.

Conflict of Interest: The authors declare that they have no conflict of interest.

Data Availability: The datasets generated and/or analyzed during the current study are available from the corresponding author upon reasonable request.

Author Contributions: I.A. - Conceptualization, Methodology, Formal Analysis, Resources, Writing – Review & Editing, Supervision, Project Administration; E.O.A. - Conceptualization, Methodology, Formal Analysis, Resources, Writing – Review & Editing, Supervision, Project Administration; B.E.O. - Investigation, Formal Analysis, Writing – Original Draft, Writing – Review & Editing; I.T. - Investigation, Data Curation, Formal Analysis, Writing – Original Draft, Writing – Review & Editing; I.M. - Investigation, Data Curation, Formal Analysis, Writing – Review & Editing; P.A.K. - Investigation, Data Curation, Formal Analysis, Writing – Review & Editing; G.O.F. - Investigation, Data Curation, Formal Analysis, Writing – Review & Editing.

AI Use Disclosure: No generative artificial intelligence tools were used in the preparation of this manuscript.

References

[1] P. Riyapan, S. Shuaib, and A. Intarasit. A mathematical model of covid-19 pandemic: A case study of bangkok, thailand. *Computational and Mathematical Methods in Medicine*, 2021:6664483, 2021. URL https://doi.org/10.1155/2021/6664483.

[2] D. Afriyie, G. Asare, S. Amponsah, and B. Godman. Covid-19 pandemic in resource-poor countries: challenges, experiences and opportunities in ghana. *Journal of infection in developing countries*, 14(8):838–843, 2020. URL https://doi.org/10.3855/jidc.12909.

[3] G. Kampf, D. Todt, S. Pfaender, and E. Steinmann. Persistence of coronaviruses on inanimate surfaces and their inactivation with biocidal agents. *Journal of Hospital Infection*, 104(3):246–251, 2020. URL https://doi.org/10.1016/j.jhin.2020.01.022.

[4] J. B. Zawilska, A. Lagodzinski, and M. Berezinska. COVID-19: From the Structure and Replication Cycle of SARS-CoV-2 to Its Disease Symptoms and Treatment. *Journal of Physiology and Pharmacology*, 72(4), 2021. URL https://doi.org/10.26402/jpp.2021.4.01.

[5] C. Owusu-Fordjour, C. K. Koomson, and D. Hanson. The Impact of COVID-19 on Learning - The Perspective of the Ghanaian Student. *European Journal of Education Studies*, 7(3), 2020. URL http://dx.doi.org/10.46827/ejes.v0i0.3000.

[6] P. T. Tabong and M. Segtub. Misconceptions, Misinformation and Politics of COVID-19 on Social Media: A Multi-Level Analysis in Ghana. *Frontiers in Communication*, 6:613794, 2021. URL https://doi.org/10.3389/fcomm.2021.613794.

[7] V. Ambalarajan, A. R. Mallela, V. Sivakumar, P. B. Dhandapani, V. Leiva, C. Martin-Barreiro, and C. Castro. A six-compartment model for COVID-19 with transmission dynamics and public health strategies. *Scientific Reports*, 14, 2024. URL https://doi.org/10.1038/s41598-024-72487-9.

[8] J. Zheng and R. Zheng. A Mathematical Modeling and Method for Predicting COVID-19-Like Infectious Disease Outbreaks. *Computational and Applied Mathematics*, 45(9):372, 2026.

[9] A. B. Celestine, A. Q. Ojoma, H. Emadifar, M. Gümüş, Shyamsunder, and A. Smerat. A Mathematical Modeling Approach to the Long-Term Global Impacts of COVID-19. *International Journal of Mathematics for Industry*, page 2650008, 2026. URL https://doi.org/10.1142/S2661335226500085.

[10] T. Izgin, S. Kopecz, and A. Meister. Recent Developments in the Field of Modified Patankar–Runge–Kutta Methods. *PAMM*, 21(1): e202100027, 2021. URL https://doi.org/10.1002/pamm.202100027.

[11] M. Djordjevic, A. Rodic, I. Salom, D. Zigic, O. Milicevic, B. Ilic, and M. Djordjevic. A Systems Biology Approach to COVID-19 Progression in Population. *Advances in Protein Chemistry and Structural Biology*, 127:291–314, 2021. URL https://doi.org/10.1016/bs.apcsb.2021.03.003.

[12] D. O. Griffin, D. Brennan-Rieder, B. Ngo, P. Kory, M. Confalonieri, L. Shapiro, J. Iglesias, M. Dube, N. Nanda, G. K. In, et al. The Importance of Understanding the Stages of COVID-19 in Treatment and Trials. *AIDS Reviews*, 23(1):40–47, 2021. URL https://doi.org/10.24875/aidsrev.200001261.

[13] S. B. Belmehdi, D. Bouagada, B. Benahmed, and K. Benyettou. On the Positivity and Stability Analysis of Conformable Fractional COVID-19 Models. *Nonlinear Dynamics and Systems Theory*, page 487, 2025.

[14] Z. Li and T. Zhang. Analysis of a COVID-19 Epidemic Model with Seasonality. *Bulletin of Mathematical Biology*, 84(12):146, 2022. URL https://doi.org/10.1007/s11538-022-01100-9.

[15] L. Jiang, J. Liang, Y. Yi, and D. Liu. Risk Propagation and Intervention in a Complex Supply Chain Network under Public Emergency. *Computers & Industrial Engineering*, page 111797, 2026. URL https://doi.org/10.1016/j.cie.2025.111797.

[16] H. H. Hussien, K. R. Genawi, N. H. Hagabdulla, and K. M. Y. Ahmed. Understanding the Basic Reproduction Number (R0): Calculation, Applications, and Limitations in Epidemiology, journal = Open Journal of Epidemiology. 15:272–295, 2025. URL https://doi.org/10.4236/ojepi.2025.152018.

[17] F. Avram, R. Adenane, G. Bianchin, and A. Halanay. Algorithmic Approach for a Unique Definition of the Next-Generation Matrix. *Mathematics*, 12(1):27, 2024. URL https://doi.org/10.3390/math12010027.

[18] I. Azure, T. Izgin, and A. Meister. Reproducibility repository for "Using Machine Learning to Enhance Hyperparameter Optimazation in Pandemic Modeling: Case study of COVID-19 Dynamics in Ghana", 2026. URL https://github.com/IzginThomas/COVID-19.

[19] T. Izgin, A. Meister, and I. Azure. Using machine learning to enhance hyperparameter optimization in pandemic modeling: Case study of covid-19 dynamics in ghana. *Journal of Mathematics in Industry*, 16(4), 2026. URL https://doi.org/10.48550/arXiv.2606.02650.

[20] S. Kopecz and A. Meister. On Order Conditions for Modified Patankar–Runge–Kutta Schemes. *Applied Numerical Mathematics*, 123: 159–179, 2018. URL https://doi.org/10.1016/j.apnum.2017.09.004.

[21] T. Izgin. *A unifying theory for Runge-Kutta-Like time integrators: convergence and stability*. PhD thesis, 2024. URL https://doi.org/10.17170/kobra-202402059522.

[22] J. K. K. Asamoah, M. A. Owusu, Z. Jin, F. T. Oduro, A. Abidemi, and E. O. Gyasi. Global stability and cost-effectiveness analysis of COVID-19 considering the impact of the environment: using data from Ghana. *Chaos, Solitons Fractals*, 140:110103, 2020. URL https://www.sciencedirect.com/science/article/pii/S0960077920305002.

[23] M. L. Diagne, H. Rwezaura, S. Y. Tchoumi, and J. M. Tchuenche. A Mathematical Model of COVID-19 with Vaccination and Treatment. *Computational and Mathematical Methods in Medicine*, 2021(1):1250129, 2021. URL https://doi.org/10.1155/2021/1250129.

[24] Isaac Azure. Structure-preserving python codes. https://github.com/a1z2u3r4e5/Structure-Preserving-Python-Codes, 2026. GitHub repository.